A MOLECULAR SCALE STUDY OF CAVITATION GROWTH AND SHOCK RESPONSE

IN SOFT MATERIALS

By

KHANDAKAR MAHMUD

Presented to the Faculty of the Graduate School of

The University of Texas at Arlington in Partial Fulfillment

of the Requirements

for the Degree of

DOCTOR OF PHILOSOPHY

THE UNIVERSITY OF TEXAS AT ARLINGTON

AUGUST 2020

To my mother

Acknowledgements

I would like to express my gratitude to Dr. Ashfaq Adnan for his constant encouragement and belief in me. At the beginning of my doctoral research, I was worried that I may quit, one to one meetings with Dr. Adnan give me hope and boost up my self-confidence. I am deeply indebted to my committee members Dr. Kent Lawrence, Dr. Hyejin Moon, Dr. Rassel Raihan, and Dr. Ye Cao who have been extremely helpful both inside and outside the class. I also want to thank Office Naval Research (ONR) for sponsoring this research work.

I must thank my parents and my only sister for their unconditional love and support. Special thanks to Riaz Kayser, Fuad Hasan, Ishak khan, Dr. Yuan Ting Wu, and Rajni Chahal for many lively and insightful discussions. Thanks to every colleague from Multiscale Mechanics and Physics Lab (MMPL) for providing valuable feedback during our group meetings. I also thank Ayesha Fatima, Delania Gordon (Lanie), and Ryan Wendy for all the administrative work. I would like to thank Michael Baker for all the technical support.

I would like to thank my friends and relatives for their continuous support.

<div align="right">August 10, 2020</div>

Abstract

A MOLECULAR SCALE STUDY OF CAVITATION GROWTH AND SHOCK RESPONSE

IN SOFT MATERIALS

Khandakar Mahmud, PhD

The University of Texas at Arlington, 2020

Supervising Professor: Dr. Ashfaq Adnan

Cavitation is a mechanism through which small vapor-filled cavities are formed in a liquid medium due to rapid changes of pressure. In liquid, the cavitation bubble is created when surrounding pressure drops below the saturation vapor pressure. Here, cavitation formation due to shock wave is considered. The molecular level heterogeneous and homogenous cavitation mechanisms and bubble growth kinetics in soft gelatin hydrogel and water has been studied. Gelatin, which is derived from collagen, is frequently used as a brain simulant material. As such, the morphology of gelatin is very different from water. In the heterogeneous cavitation study, using molecular dynamics simulation, the pressure requirement for nanoscale cavitation to grow in water and gel has been investigated. The results show that a gel-like structure requires higher pressure for the cavitation to grow, and both gel and water models exhibit a strain rate effects on the cavitation threshold pressure. The results also suggest that the cavitation collapse time is dominated by the viscosity of the medium. During the homogeneous cavitation study, the same model in the absence of preexisting bubble is stretched by volume-controlled stretching at six different strain rates. It is quite interesting to note that while critical tensile pressure for homogenous bubble nucleation of gel-like model is higher than the water at lower strain rates, at

higher strain rate the critical pressure is quite similar, thus empirical relation cannot be obtained

at much higher strain rate. The cavitation formation rate governs by the viscosity of the medium.

In the second part of the study, ECM components such as Perineuronal net (PNN) which is one

of the most prevalent components that surrounds the neuronal cell has been used to analyze the

mechanics under shock loading. Assessment of the damage efficiency of the PNN molecules at

different conditions such as shock speed, preexisting bubble, and boundary conditions have been

considered. The change of the bonding morphology which is responsible for the stability of the

secondary structure of the protein molecules of the PNN has been analyzed to evaluate the

damage level.

Table of Contents

List of Figures

Chapter 1:

Introduction

1.1 Cavitation phenomena: Study the possible cause of neuronal damage

Cavitation initiates in a liquid or soft material when the pressure drops below the saturated vapor pressure. Soft materials like gelatins are formed when interconnected collagen or collagen-like molecules form a cellular network in bulk water. A slight change in the applied pressure can collapse a cavitation bubble and induce high pressure to the adjacent cells to initiate damage. Damaging capabilities of collapsing cavitation bubbles are well known. For example, severe erosion damage to propeller blades of a sea vehicle can occur due to the high-energy cavitation bubble collapse over the blade surface. By the same mechanism, implosions in fluid-filled biological systems such as soft tissues or the brain may experience significant damage[1].

Recently, understanding the cavitation mechanisms in soft materials gained attention due to its potential implication in biomedical related applications [2][3][4][5]. Soft materials such as gelatin hydrogels are widely used as a brain simulant material [6][7][8]. Besides, the stiffness and other physical properties of gelatin gel can be tuned by changing the gel concentration in aqueous solution. Recently, reasonable structural similarities are observed between the gel network and the brain's perineuronal net (PNN)[9] (*Figure 1-1* A, B). A high-resolution cryo-SEM image shows that a gelatin microstructure consists of both crystalline and coil like amorphous part (*Figure 1-1*C), where the crystalline part is made of collagen-D periodic

microfibrillar structure [10], and the coil part, found only at the network junction, is composed of amorphous collagen chains.

Cavitation mechanisms are widely studied for water [11][12][13] and fairly well understood. However, the cavitation mechanism in the biological soft matter is not explored well. Cavitation in the gel is complicated to analyze because biological soft materials are labile and semisolid, and exhibit nonlinear elastic deformation [14]. Moreover, the interfacial tension between water and gel network may play an important role, which, in turn, may affect cavitation mechanics. At the molecular scale, the affinity of amino acid residue with water is complex because different residues have different types of interactions with water, namely hydrophobic, hydrophilic, and charged (positively or negatively). In the solution of gelatin, the crystalline collagen may interact with three types of water molecules - (a) free bulk water, (b) bound water that interacts with the gelatin surface, and (c) structural water that is trapped within gelatin molecules stabilize the triple helix [15]. In the continuum scale, surface tension and viscosity of gelatin gel are not constant, rather, they depend on gelation time and concentration [16]. Due to these structural and chemical instabilities and time-variant material properties, accurately predicting cavitation pressure for gel be very challenging.
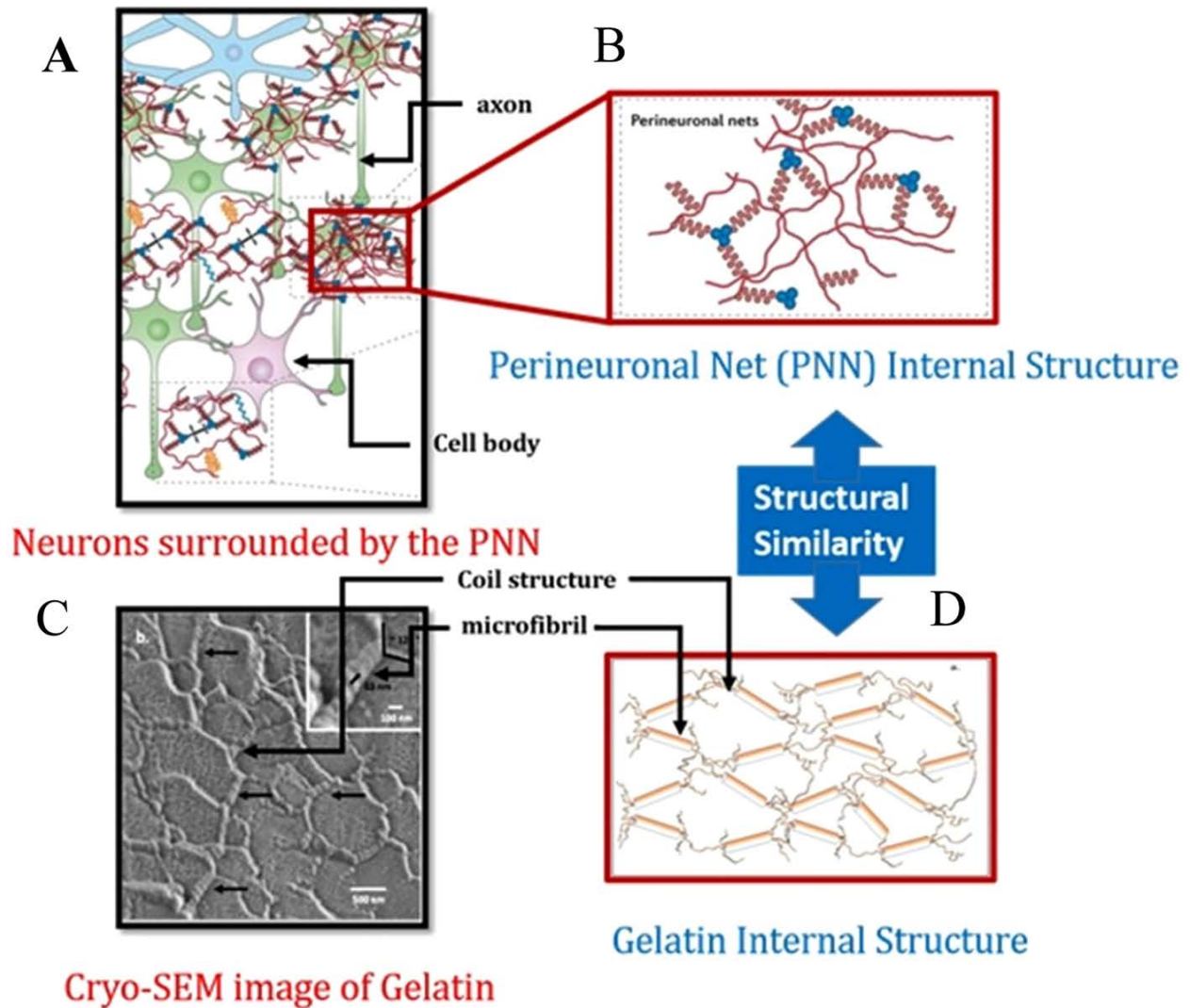
Figure 1-1 (A) Schematic illustration of perinuronal net (PNN) of central nervous system (CNS) (adapted from figure 1 of [17]) (B) schematic of gelatin network model (adapted from figure 4 of [9]) (C) Cryo-SEM image of 10% (w/w) gelatin gel with 0.5% mg/ml cross linking agent (adapted from figure 3 of [9])

Liquid water can sustain the applied negative pressure until it reaches critical pressure for cavitation. Classical nucleation theory predicts the critical negative pressure for cavitation in the

range of -140 MPa to -160MPa at room temperature[18][19][20]. However, experimentally maximum negative pressure can be reached -140 MPa in the Berthelot tube method [21]. Other experimental studies observed the critical pressure around -30 MPa using acoustic cavitation[22], shock wave techniques[23], and the method of artificial trees [24]. The experimentally observed negative pressure is far from the theoretical value, the reason behind this apparent discrepency of critical pressure requirement needs to be investigated.

Critical cavitation pressure requirement depends on several factors such as temperature, viscosity, surface tension, and cavitation time or strain rate. Among them, surface tension and temperature play a major role. The other two factors, viscosity and strain rate has been ignored due to an insignificant impact on critical cavitation pressure [18]. Very few studies explored the effect of strain rate on critical cavitation pressure of liquid water[12],[25], and soft biological materials [26]. Interestingly, Stan et al. [12] found that at the higher strain rate the bubble growth velocity is not sufficient to relax the tension, which causes more than three times higher negative pressure for bubble growth at 10 times higher strain rate. However, Fisher [18] proposed that strain rate effect is negligible, from the analytical model he found that the critical cavitation pressure changes only 1.58 times while the cavitation time ratio had changed of 10^{33} order, this claim does not necessarily depict that at all strain rates the change in the critical cavitation pressure is linear. Moreover, the viscous effect on the critical cavitation pressure has been ignored. Viscosity arises from both intermolecular and intramolecular electrostatic, Van der Waals force, and mechanical entanglement among the gel chains[27]. The critical contributing factors such as surface tension, rigidity, and viscosity affect the cavitation critical pressure.

Surface tension depends on the thermal history of gelatin, the percentage of triple helix content in gel, concentration[28], and gelation time [29]. Quenching after full denaturation of gelatin it makes hard for the coil to form a triple helix, therefore surface tension increases, because the coil has higher surface energy than triple helix. So thermal history is an important parameter to consider while characterizing a gel solution. At the same time as time progresses the triple helix content increases, irrespective of different concentrations of the solution. As a result, surface tension decreases as the gelation time increases [26]. Apart from the chemical conformation of the medium, the physical morphology of the bubble surface affects the value of surface tension. The surface tension of a perfectly flat surface is higher than the spherical surface [30].

The viscosity of gelatin is an important parameter that influences the mechanics of gel solution at different conditions. Viscosity at different concentrations can be correlated exponentially, at lower concentration (1 to 3%), the viscosity of gel does not change significantly, however, at 5 or above viscosity increases at a higher rate. The viscosity of gel significantly higher than pure water, intermolecular cohesive interaction is the key contributing factor for increased viscosity in gel [27]. Here, several interatomic forces those contribute to the increased viscosity of Gel discussed:

1. Electrostatic forces between oppositely charged ions (between mainly -COO- and $-NH_3+$).

2. Ionic-dipole forces (e.g. between -COO- on one chain and, $-NH_2$ on the other; or between $-NH_3 +$ and -COOH).

3. A Hydrogen bond between acceptor and donor (e.g. >C=0 and H-N<.)

4. London forces, between the apolar side-chains.

5. Mechanical entanglements between the long chains as found with apolar polymers in ideal solvents.

Empirical correlation of rigidity of the gelatin solution at the different concentration, average molecular weight, and temperature has been found ([31]) :

$$n^{1/2}/c = 1.22 \text{ x } 10^{-4}(M_w - 3.1 \text{ x } 10^{10} \, e^{-7900/RT})$$

Where, n, modulus of rigidity, C, concentration, M_w, is the average molecular weight of gel in solution. In a general variation of rigidity and viscosity depends on the same factor except for some fundamental difference: All the ionized side-chains of gel molecules will contribute to the viscosity, whereas the rigidity will be determined solely by those few side-chains that form intermolecular salt bridges [27].

1.2 Shock induced Damage of PNN:

Perineuronal nets (PNN) is an interconnected net-like structure which consists of three major biomolecules, such as Lectican, Tenascin-R, and Hyaluronan. The Lectican family of the chondroitin sulfate proteoglycans (CSPGs) is the most prominent in PNN of the Central Nervous System (CNS), which consists of a Core Protein (CP) with covalently connected negatively charged Glycosaminoglycans (GAGs) side chains [32]. Tenascins are globular proteins, which bind to the C-terminal domain of CP. Hyaluronan (HA) is an unsulfated GAG that is synthesized at the cell surface by the membrane-bound enzymes called HAS and protrudes through the plasma membrane into the extracellular space [33]. Hyaluronan binds to other ECM molecules via N-

terminal hyaluronan binding domains, including CP and various link proteins (LP) such as cartilage link protein, Ctrl1, and brain-derived LP such as Bral1 and Bral2 [34].

Absence of PNN in the neuron may cause a severe problem, sometimes aberrations in their molecular structure also affect the functionality of the neuron. For instance, researchers have found decreased densities of PNN, or PNN with degraded morphology, in the brain areas responsible for complex cognitive functions, such as the frontal cortex and entorhinal cortex, in subjects with Alzheimer disease (AD), suggesting that neurons with PNN alterations might be vulnerable to cell death [35]. PNN loss in AD may contribute to altered excitatory/inhibitory balance, synaptic loss, and increased susceptibility to oxidative stress [32]. Although, the trivial risk was found for veterans who had a mild TBI [36]. Some studies have also suggested that TBI is associated with an earlier onset of AD [37]. Veterans with severe TBI were 4 times more likely to have AD, whereas veterans with moderate TBI were twice as likely to have AD in late-life compared with controls [36].

The shock wave has the potential to break PNN in the presence of nano-bubbles, studies have shown that shock velocity and cavitation bubble size affect the fracture potential of PNN [5]. The higher shock speed and bigger bubble size are more damaging. Several studies have been conducted on the effect of the shock wave on the transport phenomena, deformation strain, and degradation of lipid bilayer [38]–[40]. However, the deformation mechanism of the PNN component due to shock wave has not been studied yet. The morphological degradation of PNN due to shock waves can cause several diseases and alter the action potential by damaging the synapse. Several components of PNN such as proteoglycan, tenascin-R, link protein, and

hyaluronan are vulnerable to structure altercation, among them hyaluronan which is the backbone of PNN more prone to damage [5].

In this study, different junctions of PNN which are noncovalently bonded are studied to assess their relative strength. There are three interfaces among different components of PNN, such as 1. link protein (LP) Core Protein (CP) of proteoglycan (PG), 2. Tenascin-R (TR) and CP, 3. LP and Hyaluronan (HA). The relative strength of the junctions has been evaluated to figure out the weakest junction among the molecular interfaces of the PNN. Afterward, damaging efficiency of the shock wave propagation through the PNN model has been studied.

1.3 Motivation for work:

1.3.1 Feasibility of cavitation in GEL

Cavitation mechanism in water is well understood [11][12][13]. Few studies are available on cavitation of soft viscoelastic materials such as gelatin [7], polyacrylamide hydrogels[41], etc. Wonmo Kang et al.[7] observed that cavitation pressure sharply rises in 1 % gelatin solution when compared with pure water (*Figure 1-2*). It has been hypothesized that the rise in cavitation threshold in the gel is due to the higher surface tension, preexistence thermal residual stress, and nonspherical bubble formation in the gel. There might have other reasons such as interfacial tension, stiffness of gel fibril, and material properties such as Density, viscosity, and surface tension that may play a critical role during growth and collapse of the bubbles.
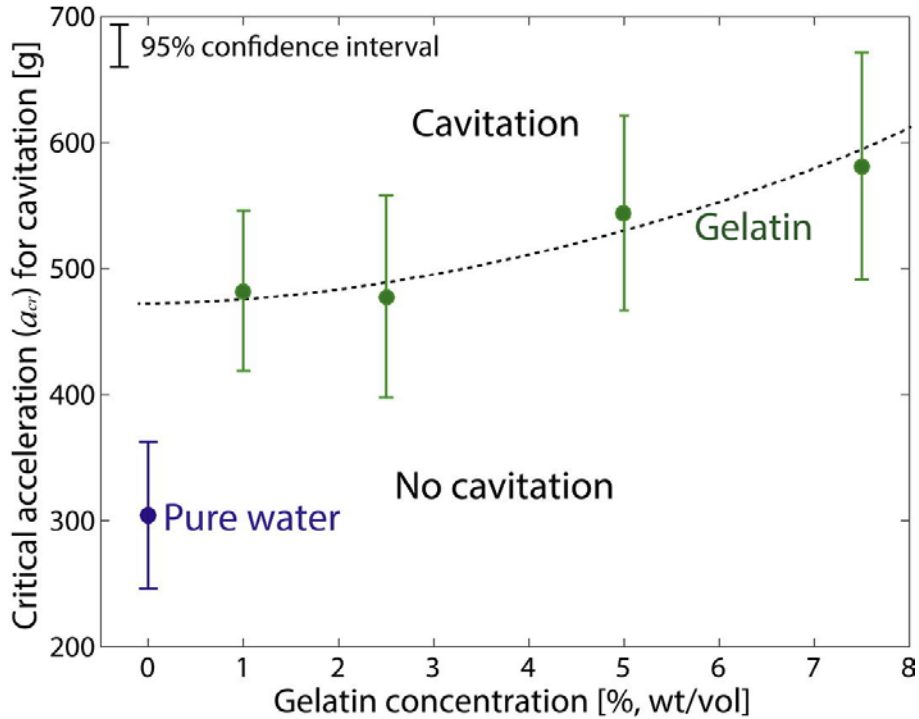
Figure 1-2 The critical acceleration corresponding to cavitation nucleation at room temperature

as a function of gelatin concentration (weight per volume percentage, gram/milliliter) [7].

1.3.2 Shock induced damage of PNN

Impact load during a car accident at 30 MPH generates a G force around 30g, NFL player during the collision may experience as high as 150g, similarly, soldiers impacted by improvised bomb blast may experience severe g force. A Human being can survive around 46 g force without any major damage. The acceleration profile of a collision is shown in Figure 1-3a, the rapid deceleration is fatal. Roughly, 90 to 100 g-force causes concussion (Figure 1-3b). Concussion, sub concussions, and exposures to the shock waves from the explosive blast can cause Mild traumatic brain injury (mTBI) [36].

The initial blast-generated shock wave profile features a sudden increase in pressure, often referred to as overpressure, followed by a low magnitude long-range negative pressure tail [42]. For example, the major ingredient in RDX (Royal Demolition eXplosive) can generate an initial overpressure of over 27 GPa [43]. The long-range negative pressure tail causes damage to the Extra-Cellular Matrix (ECM) and neuronal cells by forming micro cavitation [42] and mechanical fracture of different biomolecules [4], [5]. The overpressure generates a compressive load which may cause shear fracture of biomolecules. The blast-induced damage is schematically illustrated in *Figure 1-4*. Perineuronal net (PNN) is an important component of ECM which Give Neuroprotection, regulate synaptic plasticity, and protect neuron cell from Oxidative stress. Therefore, the investigation of the behavior of PNN under shock loading is important.

10

(g's) 0 10 20 30 40 50 60 70 80 90 100 110 120 130 140 150

Walking: 1.0
Sneezing: 2.9
Shuttle launch: 3.0
Coughing: 3.5
Slap on the back: 4.1
Roller coaster: 5.0
Hopping off a step: 8.1
F-16 fighter jet roll: 9.0
Concussion: 100
Impact: 150
Extreme football

b
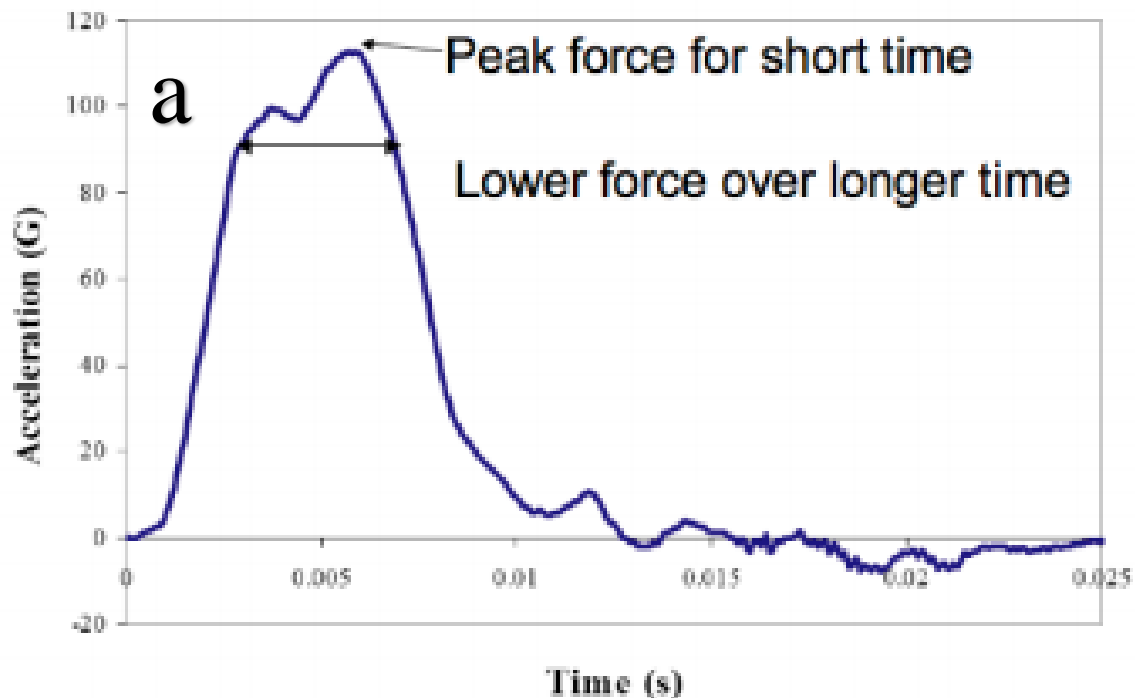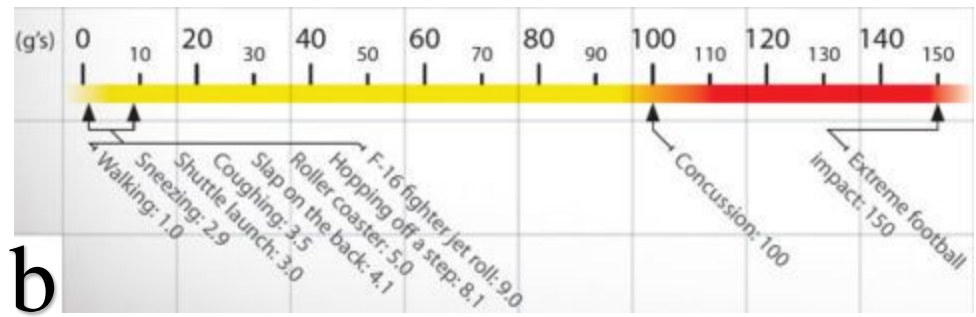
Figure 1-3 (a) Acceleration profile in materials due to the shock wave. Rapid deceleration is

fatal. (b)Average G values at different conditions
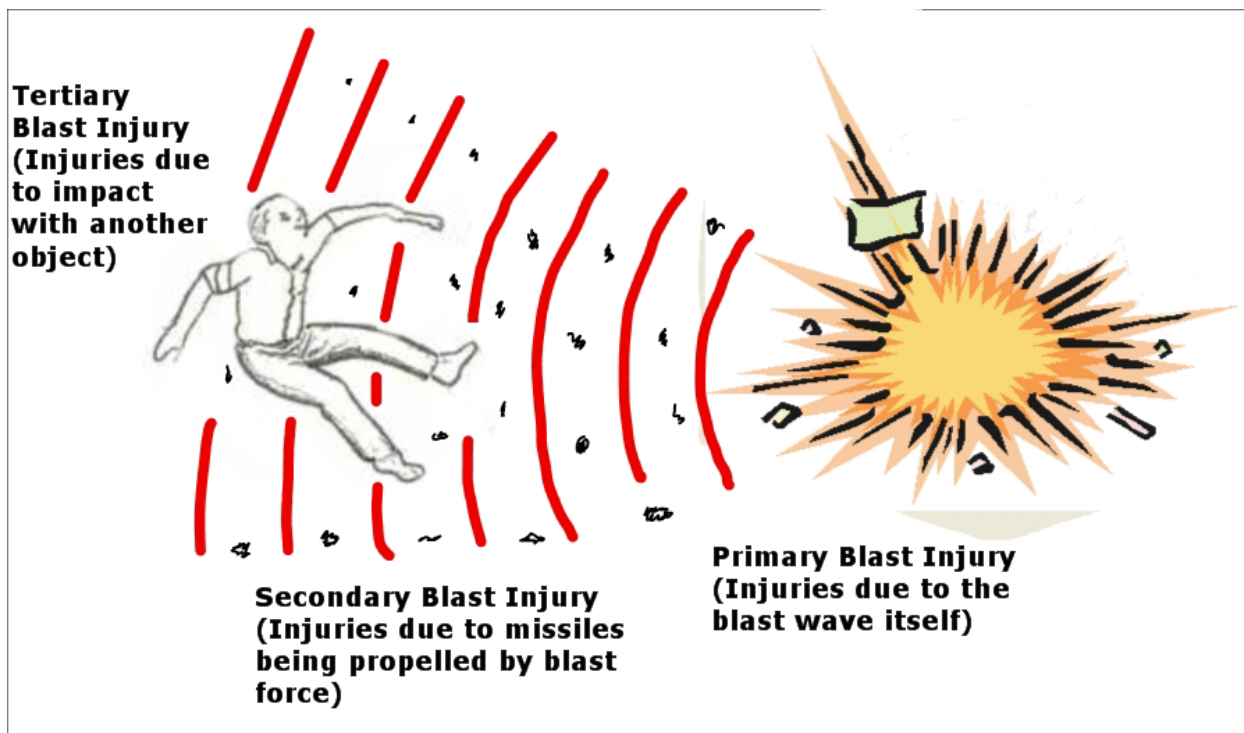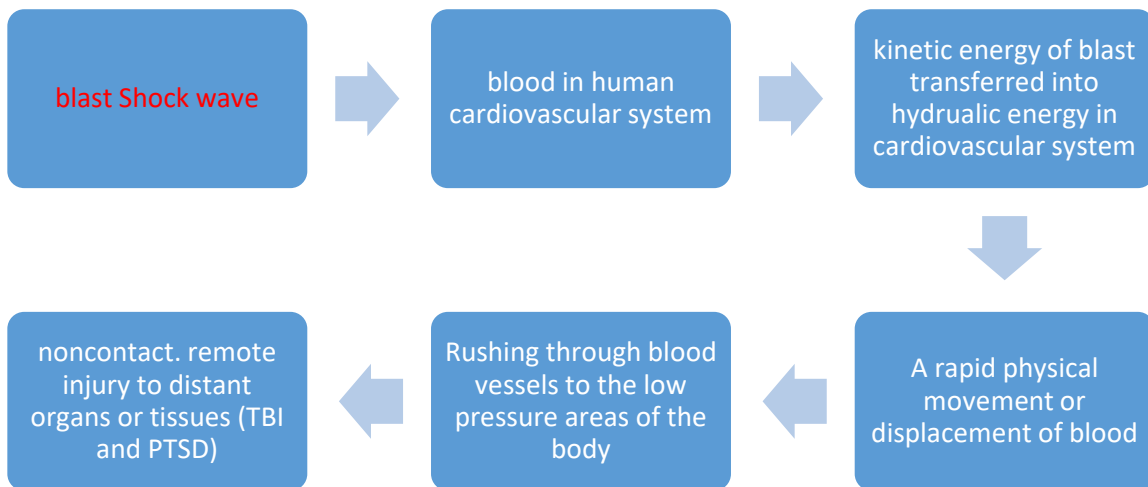
Figure 1-4 (a) shock-induced damage flow path in the human body [44] (b) schematic illustration of blast injury [43]

1.4 Objectives and Outline of the thesis

1.4.1 Cavitation in GEL

The objective of this study is to determine the underlying molecular mechanism of cavitation in water and gel-like soft materials. It has been found experimentally that cavitation pressure in gelatin gel is higher than that in water (*Figure 1-2*), however, the exact mechanism of cavitation is still unclear. The goal of this study is to investigate the possible cavitation mechanism in gelatin by atomistic simulation. The physical properties of liquids such as surface tension, viscosity, and density play a vital role in the bubble dynamics. Evaluation of these important properties is the key to determine the underlying cavitation mechanics in water and gel-like materials. Cavitation growth in the presence of a preexisting bubble is called heterogeneous cavitation and in absence of it called homogeneous cavitation. Determine the critical pressure for the homogenous and heterogeneous cavitation and the associated mechanism is the key objective. Other simulation parameters such as strain rate may affect the critical pressure.

The research goal is to fulfill the following objectives:

- Compare the bubble dynamics in water with GEL

- Measure the pressure needed to enable cavitation in water and GEL

- Evaluate the bubble collapsing mechanism

- Differentiate the homogenous and heterogeneous cavitation mechanism in GEL and water

1.4.2 Shock Induced Damage of PNN

PNN is a protective net-like structure that has significant function on neuronal activity such as neurotransmission, charge balance, and generate action potential. Shock induced damage of this essential component may cause neuronal cell death and potentially leads to CTE, AD diseases, PTSD, etc. The shock generated during an accident, improvised bomb blast, or during the collision of NFL players may lead to damage to this safety net. The goal is to investigate the mechanics of PNN under shock wave. To understand the mechanics of PNN, mechanical properties of different PNN components such as glycan, GAG, and protein need to be evaluated. Average pressure experienced by different components at different shock speed is one of the key parameters to access the damage criteria of PNN. The effect of the preexisting bubble may enhance the damage by producing shock jet in the system. Therefore, in this study effect of the preexisting bubble, speed of shock wave and boundary condition of the PNN has been taken into account to access the damage criteria and mechanism.

The research goal is to fulfill the following objectives:

- Evaluate the deformation strength of PNN components and interfacial strength between PNN components.
- Investigate the pressure profile of the components at different shock speed
- Finding out the damage efficiency of a shock wave at different speeds and access the failure mechanism

1.4.3 Outline of the thesis

In this study, two different but integrated topic is discussed. At first, the physics of bubble growth and collapse in a molecular scale for water and gel-like model is investigated. Both homogenous and heterogeneous cavitation is discussed. Secondly, the damage mechanism of the shock wave to the essential ECM components such as PNN has been studied. In Chapter 2, the methodology of bubble growth and collapse simulation is presented. In addition to the simulation protocol, the fundamental mathematics of atomistic simulation and different force fields have been discussed briefly. In the later part of this chapter, gel-like model building methodology, simulation and post-processing protocols are discussed. In Chapter 3, the results of bubble dynamics are presented and discuss the physics of heterogeneous and homogenous cavitation. In chapter 4, the building methodology of the PNN model and protocol of shock simulation is presented and post-processing methodology is discussed. In Chapter 5, the results of the mechanical strength of PNN components and shock simulation are presented and discussed. Finally, In Chapter 6, the conclusion of the findings is presented and possible outline of future work is proposed.

Chapter 2:

Methodology: Cavitation in Gel

2.1 Molecular dynamics (MD) Simulation:

MD simulation mimic what atoms do in real life, atoms of different types of materials maintain potential energy function. The energy function allows the calculation of the force experienced by any atom given the positions of the other atoms. Newton's second law of motion tells how the forces will affect the motion of the atoms. During the MD simulation process, the solver numerically calculated the position of each atom in every timestep. Timestep (δ_t) should not exceed more than 2 femtoseconds. Equation (2-1) and (2-2) shows the straight forward numerical solution for the position of each atom at a given time for a forcing function. It is known, forcing function, $F(x) = -\nabla U(x)$, a function of potential energy, the potential energy is evaluated from the interaction potential of different atoms.

$$x_{i+1} = x_i + \delta_t v_i \tag{2-1}$$

$$v_{i+1} = v_{i+1} + \delta_t F(x_i) / m \tag{2-2}$$

Detail discussion of the MD algorithm is out of the scope of this research, if the reader wants to learn more about MD algorithm and statistical mechanics can refer to this reference [45].

2.2 Force field for biomolecules

Several Force Fields (FFs) are widely used that have rigorously determined parameter sets for aqueous protein simulations—the CHARMM [46], AMBER [47], GROMOS [48], OPLS [49], and ReaxFF [50] FFs are among the best known. In this work, CHARMM36 FF and ReaxFF force field are used, because those have been used in many aqueous protein solution dynamics. In molecular dynamics simulations, at femtosecond time interval the positions of the atoms are updated, the positions are determined based on the forcing functions that include bonded and nonbonded interaction [51]. All the biophysical FFs mentioned above use a similar potential energy function for the energy calculations except ReaxFF. ReaxFF is a reactive force field where bond breakage is taken into account. In this study, the ReaxFF force field is used for those molecules failure or fracture analysis are needed, otherwise, CHARMM36 forcing potential is used.

2.2.1   CHARMM36 force-field:

The potential energy function in the CHARMM FF is

$$
\begin{aligned}
U_{\text{total}} = &\sum_{\text{bonds}} K_b(b - b_0)^2 + \sum_{\text{angles}} K_\theta(\theta - \theta_0)^2 + \sum_{\text{UB}} K_{\text{UB}}(S - S_0)^2 \quad (2\text{-}3) \\
&+ \sum_{\text{dihedral}} K_\chi(1 + \cos(n\chi - \delta)) + \sum_{\text{impropers}} K_{\text{impr}}(\varphi - \varphi_0)^2 \\
&+ \sum_{\text{LJ}_{i \neq j}} \varepsilon_{ij}\left[\left(\frac{R_{\text{min}_{ij}}}{r_{ij}}\right)^{12} - 2\left(\frac{R_{\text{min}_{ij}}}{r_{ij}}\right)^{6}\right] + \sum_{\text{coulomb}} \frac{q_i q_j}{\varepsilon_i r_{ij}},
\end{aligned}
$$

The CHARMM36 force field contains bonded and nonbonded interaction potentials. The CHARMM36 forcefield potentials define the optimum values of the bond, angle, dihedral, and improper angles and their coefficient.

Bonded Interactions: Different bonded interactions are presented in Figure 2-1. Bonds are described by a harmonic potential V_{bond} (R) with an equilibrium distance R_{bond} and a force constant of K_{bond} (Eq (2-4)). Bonded particles are somewhat closer to each other than neighboring nonbonded particles. To represent chain stiffness, a weak harmonic potential V_{angle} (θ) is used for the angles. The equilibrium angle remains at Θ_0 degrees (Eq(2-5)). Dihedrals represent conformational flexibility in biomolecules and the energy of rotation around a covalent bond. In Figure 2-1C, ϕ is the angle between the plane containing the first three atoms in the dihedral and the plane containing the last three. The ``multiplicity'' n is typically 1, 2, or 3, although for a small number of cases two or three terms with different values of n are provided for the same atom types (Eq (2-6)). The final bond-like terms in the parameter file are impropers, which are used exclusively and explicitly in the molecular topology to maintain planarity. As such, the harmonic form of the improper angle with a large spring constant and typically zero is used to restrain deformations among an atom and three atoms bonded to it. As with dihedrals, Ψ is the angle between the plane containing the first three atoms and the plane containing the last three (Eq (2-7)) [52].
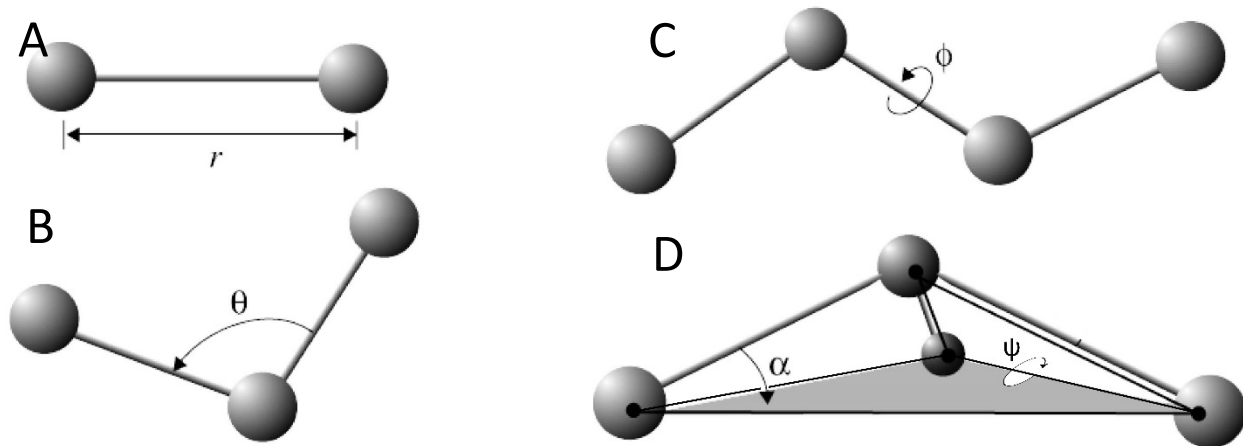
Figure 2-1 Bonded interaction: (A) Bond between two atoms, (B) Angle between three atoms,

(C) Dihedral angle between four atoms and (D) Improper-dihedral angle of four atoms [52]

$$V_{bond}(R) = \frac{1}{2}K_{bond}(R - R_{bond})^2 \qquad (2\text{-}4)$$

$$V_{angle}(\theta) = \frac{1}{2}K_{angle}[\cos(\theta) - \cos(\theta_0)]^2 \qquad (2\text{-}5)$$

$$V_{dihedral}(\phi) = \frac{1}{2}K_{dihedral}[1 + \cos(n(\phi - \delta)]^2 \qquad (2\text{-}6)$$

$$V_{improper}(\Psi) = \frac{1}{2}K_{\Psi}[\Psi - \Psi_0]^2 \qquad (2\text{-}7)$$

Non-bonded Interactions: Lennard-Jones (LJ) 12-6 potential energy function is used to describe the non-bonded interaction which is called Van der Waals interactions, with σ_{ij} representing the closest distance of approach between two particles and ϵ_{ij} the strength of their interaction Eq (2-8). Van der Waals interactions are truncated at the cutoff distance. A smooth switching function is used to truncate the Van der Waals interaction at the cutoff distance. A graph of the van der Waals potential with this switching function is shown in *Figure 2-2* A. If switching is set to off, the van der Waals energy is just abruptly truncated at the cutoff distance, so that energy may not be conserved.
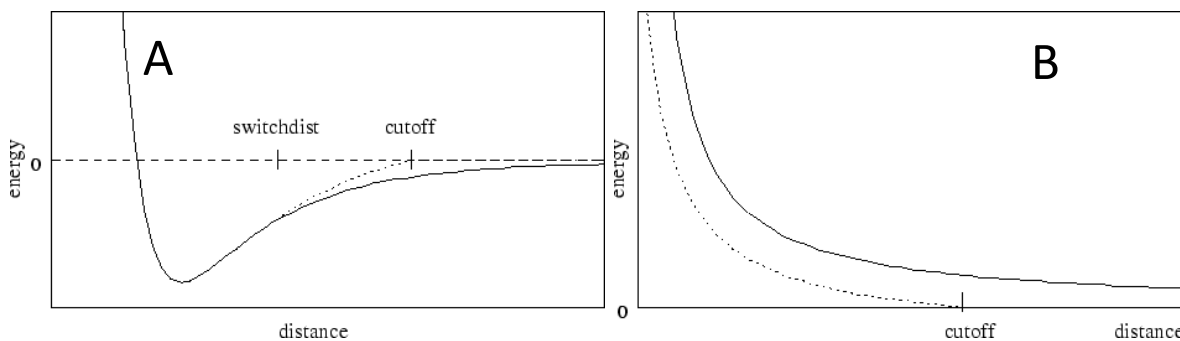
Figure 2-2 Non-bonded interaction: (A) Van der Waals interactions (B) Electrostatic interactions

The handling of electrostatics is slightly more complicated due to the incorporation of multiple time-stepping for full electrostatic interactions. There are two cases to consider, one where full electrostatics is employed and the other where electrostatics are truncated at a given distance.

First let us consider the latter case, where electrostatics are truncated at the cutoff distance. Using this scheme, all electrostatic interactions beyond a specified distance are ignored, or assumed to be zero. If switching is set to on, rather than having a discontinuity in the potential at the cutoff distance, a shifting function is applied to the electrostatic potential as shown in *Figure 2-2* B. As

this figure shows, the shifting function shifts the entire potential curve so that the curve intersects

the x-axis at the cutoff distance.

$$U_{LJ}(r) = 4\epsilon_{ij}[(\frac{\sigma_{ij}}{r})^{12} - (\frac{\sigma_{ij}}{r})^6] \tag{2-8}$$

$$U_{el}(r) = \frac{q_i q_j}{4\pi\epsilon_0\epsilon_r r} \tag{2-9}$$

2.2.2   ReacxFF:

A fundamental assumption of ReaxFF is that the bond order BO'_{ij} between a pair of atoms can be

obtained directly from the interatomic distance r_{ij} as given in equation (2-10) and plotted in

Figure 2-3. Equation (2-10) consists of three exponential terms: (1) the sigma bond ($P_{bo,1}$ and

$p_{bo,2}$) which is unity below ~1.5 Å but negligible above ~2.5 Å; (2) the first pi bond ($P_{bo,3}$ and

$p_{bo,4}$) which is unity below ~1.2 Å and negligible above ~1.75 Å, and (3) the second pi bond

($P_{bo,5}$ and $p_{bo,6}$) which is unity below ~1.0 Å and negligible above~1.4 Å. For details on force

field energy calculation, you may refer to this paper [50] by Van duin et al.

$$BO'_{ij} = exp\left[P_{bo,1}\left(\frac{r_{ij}}{r_o}\right)^{p_{bo,2}}\right] + exp\left[P_{bo,3}\left(\frac{r_{ij}^{\pi}}{r_o}\right)^{p_{bo,4}}\right]$$
$$+ exp\left[P_{bo,5}\left(\frac{r_{ij}^{\pi\pi}}{r_o}\right)^{p_{bo,6}}\right] \tag{2-10}$$
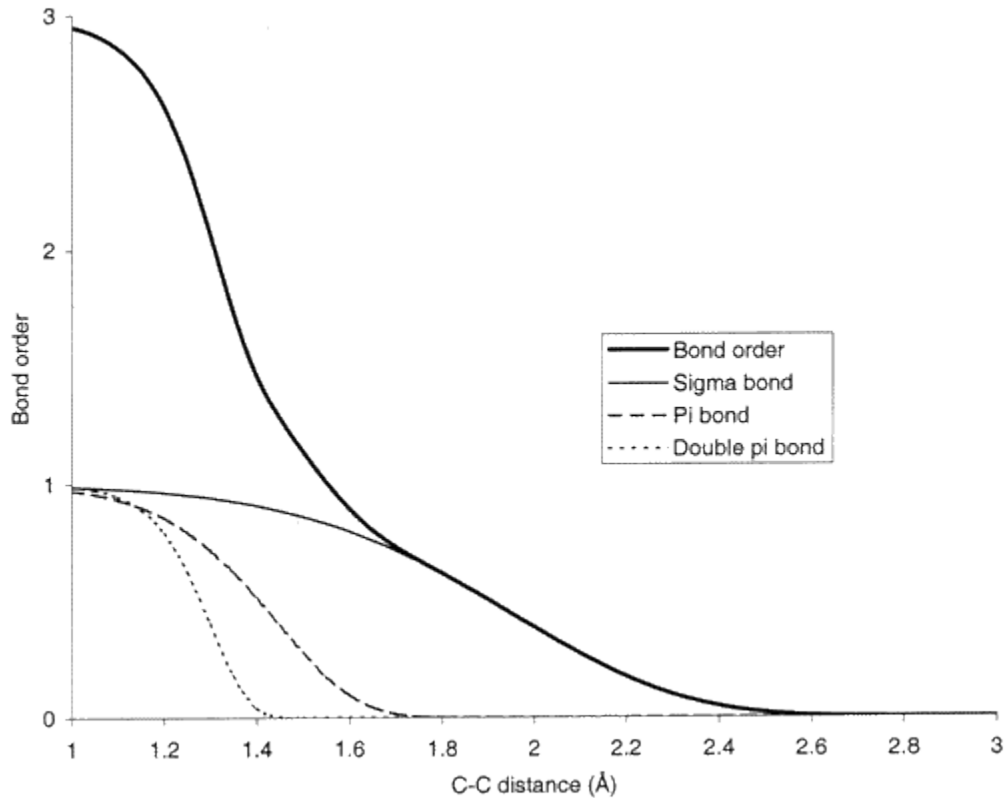
Figure 2-3 ReaxFF: Interatomic distance dependency of the carbon−carbon bond order [50].

2.3 Models for mechanical property evaluation

2.3.1   Building Gel Like model

Collagen structure (Protein Data Bank identification code 3HR2) used for this study is obtained

from the author of this work [53] . The Homology modeling approach is adopted to build the

protein model using modeler software. The collagen triple helix is 3000Å in length and ~15 Å in

diameter. Only part of the full triple helix of 200Å length collagen molecule is taken simply by

editing the PDB file. A hexagonal array of microfibril like structures has been built by placing

seven triple helices at six corners of the hexagon and one in the center point of a hexagon by

using UCSF chimera protein visualization software [54]. To replicate a hydrogel like structure the microfibril structure is further edited to remove few alpha 1 and alpha 2 chains from the triple helix. The mid 100Å along the length direction is more of like coil and 50Å from both ends is more like the micro-fibril like structure (*Figure 2-4*).
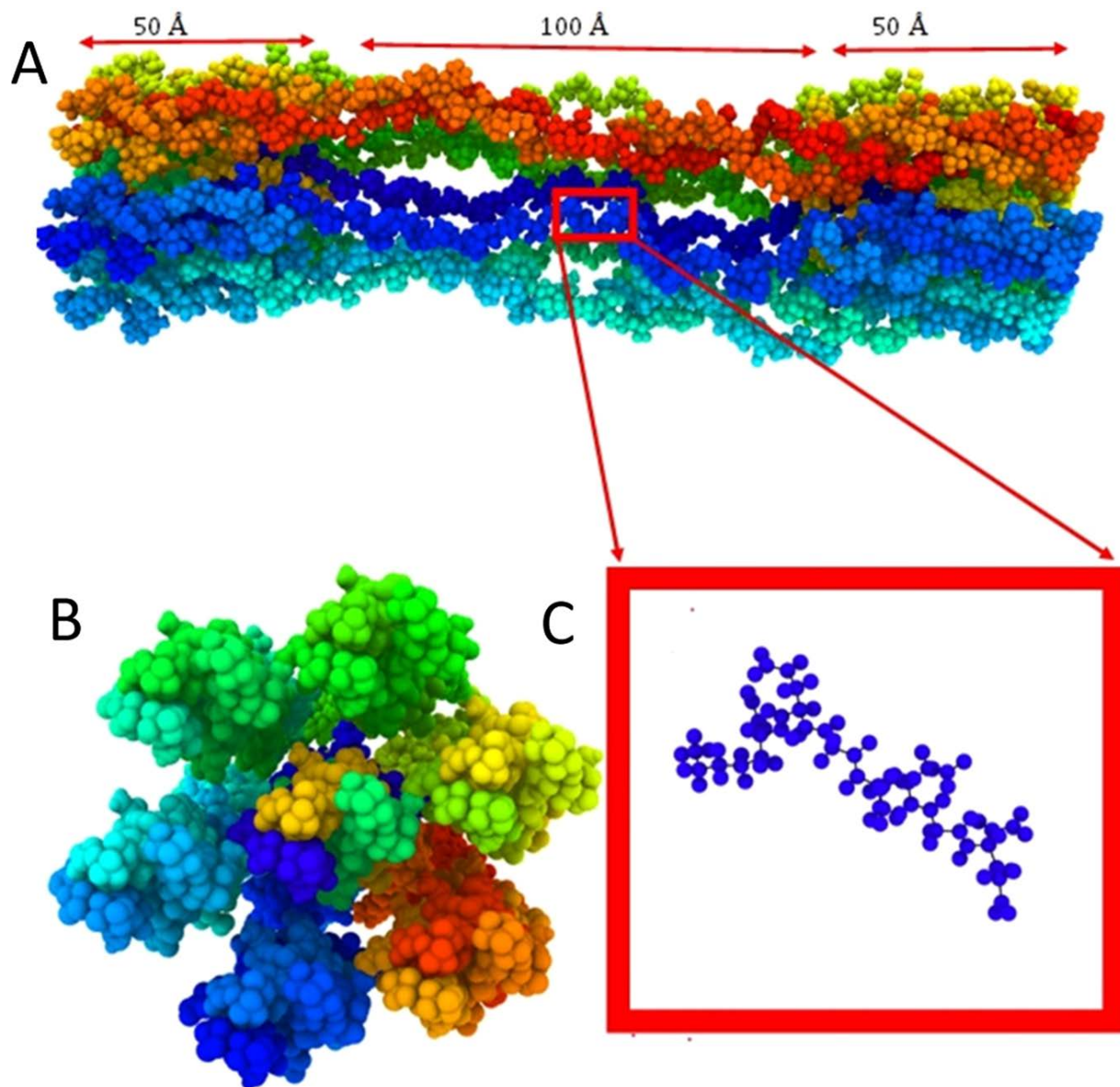
Figure 2-4 Gel Model (A) Full model of gel fibril (B) Cross-sectional view of fibril (C) Individual coil profile

2.3.2 Atomistic model of Gel-like structure for cavitation study

The cavitation simulation model is designed by simply copying the gel-like microfibril model at different positions of the box ($211 \times 211 \times 165$). While placing the gel-like model some rotation and translation is applied by UCSF chimera. All models are solvated by TIP3P water using CHARMM-GUI [52] Solvator. Two models are created of the same box dimensions, where the percentage of collagen is 10.4 % w/w, and 0% w/w respectively (shown in *Figure 2-5*). Bubbles are created by deleting some water molecules in the middle of the box of 50Å radius.
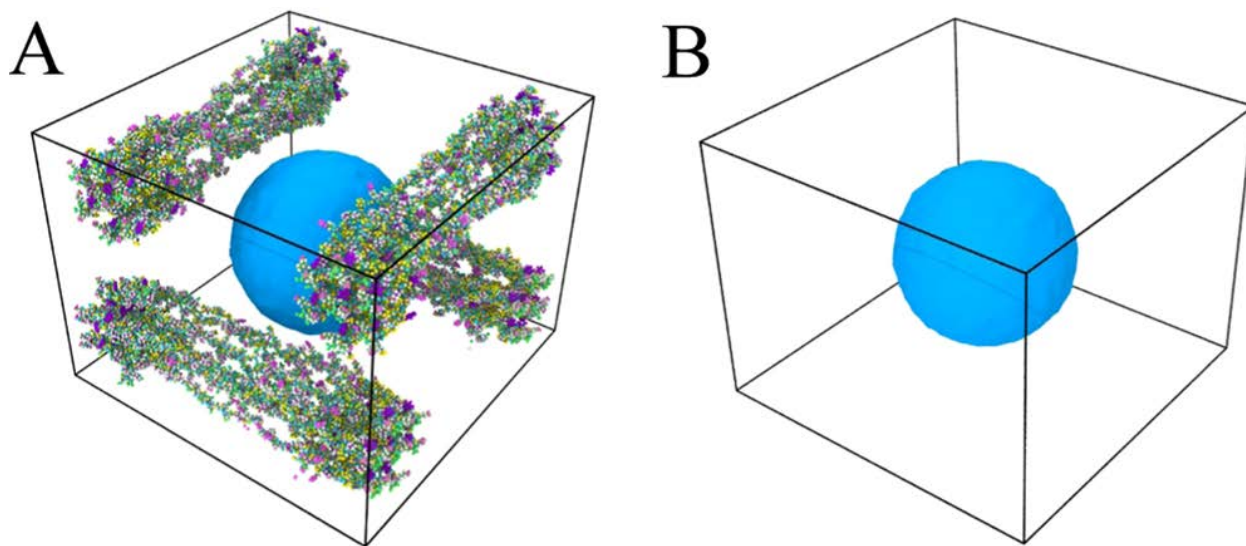
Figure 2-5 Models for cavitation study (A) Gel like model (B) Water

2.4 Mechanical Property evaluation

2.4.1 Mechanical Strength of Gel like structure

The mechanical property is evaluated of collagen molecules by steered molecular dynamics (SMD) simulation at different scales such as single coil, double coil, triple helix, and gel-like

structure (Figure 2-6). Each structure is 100 Å in length except the gel like structure. To maintain constant strain rate gel like structure is pulled at twice as much as the triple helix pulling velocity. In SMD approach constant velocity is applied for all cases, with appropriate spring constant (Figure 2-6C). All the SMD simulation is carried out at the NVT ensemble at constant strain rate.
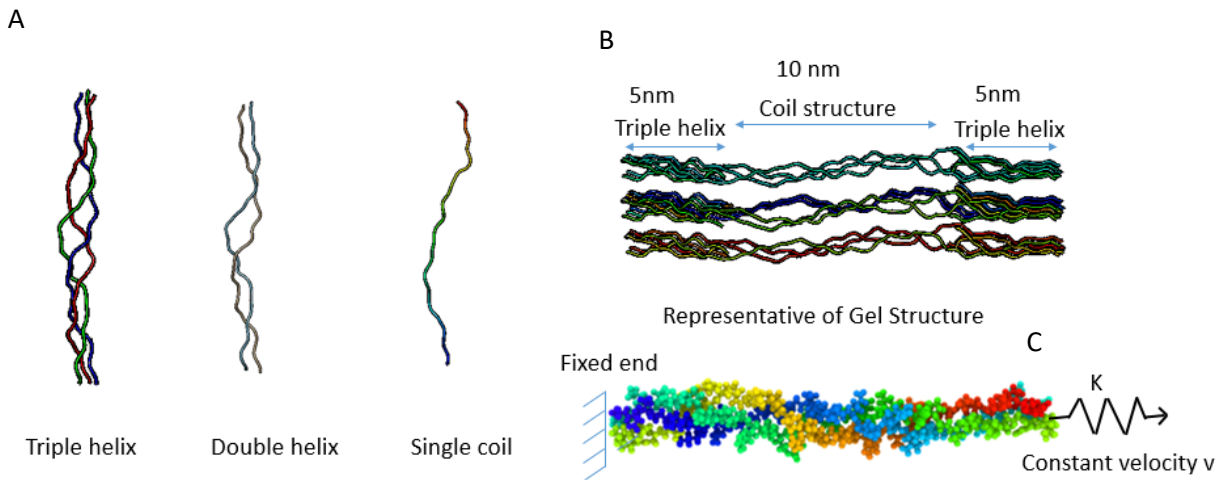
Figure 2-6 Collagen profile at different scale (A) collagen segmented profile (Triple helix, double helix, coil) (B) Gel-like structure for our model to study cavitation (C) SMD pulling approach for strength determination

2.5 Cavitation study

For cavitation study, isostatic pressure is applied by applying a constant volume expansion rate. Rate dependency on cavitation pressure is examined by the application of volume expansion at two different strain rates (X and 2X). Bubble radius is measured by the ovito "construct surface mesh" tool at different timesteps. The movement is restricted to the end chain c-alpha atom

during the cavitation study and uniform deformation is applied to the water molecules only. Stress/atom is calculated to measure the pressure. Stress/atom gives the value of (stress x volume) in each direction for each atom, dividing by volume of each atom gives us the exact amount of virial stress. Global pressure, $P = (Pxx + Pyy + Pzz)/(3 \times V)$, where Pxx, Pyy, and Pzz is the summation of stress/atom value for all atoms in x, y, and z direction respectively and V is the summation of each atom's volume in the system. For volume measurement, the voronoi cell is created around each atom using Voro++ package [55] which is compiled in LAMMPS.

2.6 Simulation parameters

The interatomic potential has been adopted from the CHARMM force field [51] and the simulation is carried out by LAMMPS [56] and GROMACS [57] open-source software package on TACC supercomputer (STAMPEDE2 and Lonestar5). For visualization of LAMMPS trajectory file OVITO [58] and VMD [59], visualization software is utilized. MATLAB is used for data analysis.

All models are equilibrated for sufficient time until the potential energy became stable in isothermal-isobaric (NPT) ensemble, where Nose-Hoover thermostat is applied to equilibrate at a constant temperature, and Nose-Hoover barostat is applied to equilibrate pressure to zero (ATM). Lenard jones pair style is used with standard inner and outer cutoff. Long-range coulombic interactions are computed by pppm style which invokes a particle-particle particle-mesh solver which maps atom charge to a 3d mesh, uses 3d FFTs to solve Poisson's equation on the mesh, then interpolates electric fields on the mesh points back to the atoms. A Periodic boundary condition is applied at all three directions.

Chapter 3:

Mechanical stiffness and cavitation pressure correlation

3.1. Mechanical Strength of gel like structure

For the stretching simulation, triple helix, double helix, single coil, and gel-like structures are pulled at a constant strain rate. After equilibration, constant velocity is applied along the longitudinal direction. The gel-like structure and triple helix shows maximum and minimum shrinkage respectively during equilibration. The required pull force is evaluated by the MD simulation study (SMD approach), where constant velocity is applied from one end, and another end remained fixed. The schematic is shown in the inset picture of Figure 3-1. The Average cross-sectional area is analyzed by Fiji ImageJ [60] image processing software.

The results are reported in Figure 3-1, it has been found that triple helix is the stiffest among the configurations tested. The triple helix is the coiled-coil structure which gives it more stiffness as compared to other configurations tested. Double helix got intermediate stiffness since it is a metastable structure, during simulation double helix can retain the coiled-coil configuration that gives additional stiffness although lower than the stable triple helix configuration. The gel-like structure behaves more like the coil structure while pulling at the beginning it shows more stiffness than the coil. The gel-like structure end (which is pulled and fixed) is more like a triple helix, therefore, shows similar stress-strain trend as the triple helix at the toe region, however after the stress is transferred to the weakest part that is the coil-like structure, it behaves like the coil structure. Because of this discrepancy modulus is calculated from 0.04 to 0.14 strain value for both the coil and gel-like structure.
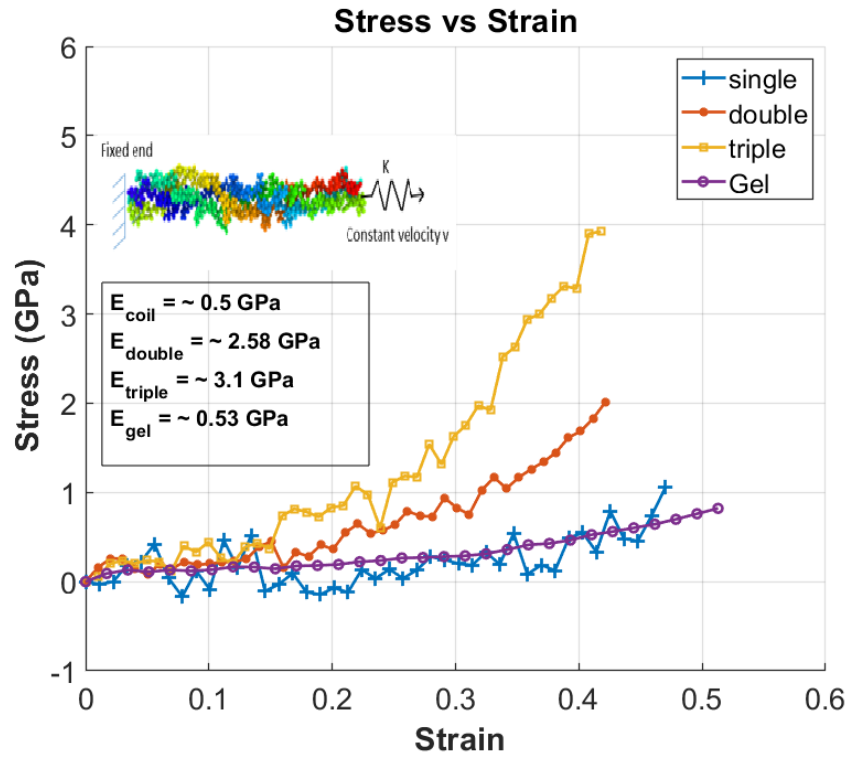
Figure 3-1 stress strain comparison of coil, double helix, triple helix and Gel like structure

3.2. Heterogenous Cavitation

3.2.1 Bubble growth

It is known that when a pure liquid, such as water, is allowed to expand at a constant rate, at some point, a tiny void (or many voids at the same time) will form inside of the pure liquid. The equilibrium is maintained through the balance of surface tension and the applied tensile (expansion) pressure. In the cavitation community, the tensile pressure is often referred to as negative pressure. In the absence of vapor pressure, the equilibrium equation for the stable bubble is[61]

$$\frac{2S_{liq}}{R} + P_{cav}|_{liq} = 0 \qquad \text{(3-1)}$$

Where, $P_{cav}|_{liq}$ = required far-field pressure for a stable bubble in a pure liquid, S_{liq}=surface tension of the liquid, and R= stable bubble radius.

The presence of a network in gel consumes additional strain energy that must be overcome for the growth of the cavitation. As such, the required cavitation pressure in gel $P_{cav}|_{gel}$ would be higher than $P_{cav}|_{liq}$. Qualitatively, this relation can be written as

$$\frac{2S_{gel}}{R} + P_{cav}|_{gel} = 0 \qquad \text{(3-2)}$$

Where, $P_{cav}|_{gel} = P_{cav}|_{liq} + P_{cav}|_{network}$, where, $P_{cav}|_{network}$ is the pressure equivalent of the additional strain energy (bending, tensile, and torsoinal) [62] associated with the gel network deformation and S_{gel}, is the surface tension of gel.

Once the bubble is nucleated, it then continues to grow as long as the condition for bubble growth is maintained. Here, the molecular level cavitation growth phenomena in water and gel-like structures have been studied. The gel model is built on four collagen fibrils that are arranged in a network forming architecture and immersed in water molecules. The fibrils are placed at the top and bottom surface of the model (*Figure 2-5*A). The gel-like structure has approximately 10.4 % (w/w) collagen molecule. To simulate cavitation growth, a uniform hydrostatic tensile

(negative pressure) stress is induced to the system by increasing the system volume at a strain

rate of X=6.7 × 10^9 s^{-1} and 2X=1.35 ×10^{10} s^{-1}, respectively. The application of the uniform tensile

pressure implies an overall increase in the system volume. Note that system volume (V_{system})

includes water volume (V_{water}), the bubble volume ($V_{bubble}=\frac{4}{3}\pi R^3$) and gel network ($V_{network}$),

as written below

$$V_{system} = V_{water} + V_{network} + V_{bubble} \tag{3-3}$$

The cohesive energy between water molecules always tries to maintain equilibrium water

density. Since the gel network is immersed in water, it will not expand during the system

expansion. As such, during system expansion, water will initially expand but eventually, the

system expansion will become proportional to bubble volume expansion or bubble growth. The

results are shown in Figure 3-2 for the X strain rate. It has been found that the presence of the

collagen network requires additional pressure to grow cavitation in the "gel" system when

compared with cavitation bubble growth in the water model (Figure 3-2A), density variation

follows the same trend as pressure (Figure 3-2B). The process, in principle, supports Eqn.(3-2).

To discuss the molecular mechanisms in detail, the bubble growth process is divided into three

distinct regions (See Figure 3-2C).

Region 1: (0-12 ps) Here, the growth rate is very slow. Note that the cavitation is created by

introducing a new surface (i.e. by removing a water sphere from the center of the rectangular

system). As such, two opposing forces simultaneously act – (i) a favorable expansion force that

tends to grow the bubble, and (ii) a surface tension force that tends to shrink the bubble. These two competing forces are strong at the beginning; hence, the velocity of bubble growth is very low. As the bubble grows further, the surface tension effect starts to become less dominant. When the bubble crosses the threshold pressure, a sharp rise in pressure is observed. At this stage, the velocity of bubble growth is maximum (Figure 3-2 C)

Region 2: (12-25 ps): In this region, there is a sharp rise of negative pressure where the work input by volume expansion overcomes the opposing force due to surface tension. The rise in pressure is more pronounced in water than gel because gel is nearly three times more viscous than water (see Table 3.1). The viscosity of water and gelatin system is measured; the methodology is described in "Appendix B: Viscosity Measurement" of supplementary materials. The study of viscosity measurement is well fitted with the empirical correlation (second-order polynomial) of viscosity and concentration, studied by Cumper et al. [27]. It has been noticed that the magnitude of negative pressure in the water near the end of region 2 reduces to its initial value (-20MPa). The bubble volume to box volume ratio in this region is the highest, therefore, a decrease in tensile pressure is observed. Shortly afterward, it gradually starts to become stable.

Region 3: (25-60 ps): In this region, the bubble growth rate is stable for both the systems. It is observed that pressure fluctuates at higher frequencies in water. The oscillatory nature of pressure fluctuation can be explained from the structural dynamics point of view. It has been discussed the dynamics of the bubble in "section 3.2.2" in more detail. Moreover, in this region, the sphericity index of the bubble (Figure 3-2D) in the gel system deviates from the water bubble, which gives us an indication of bubble network interaction.
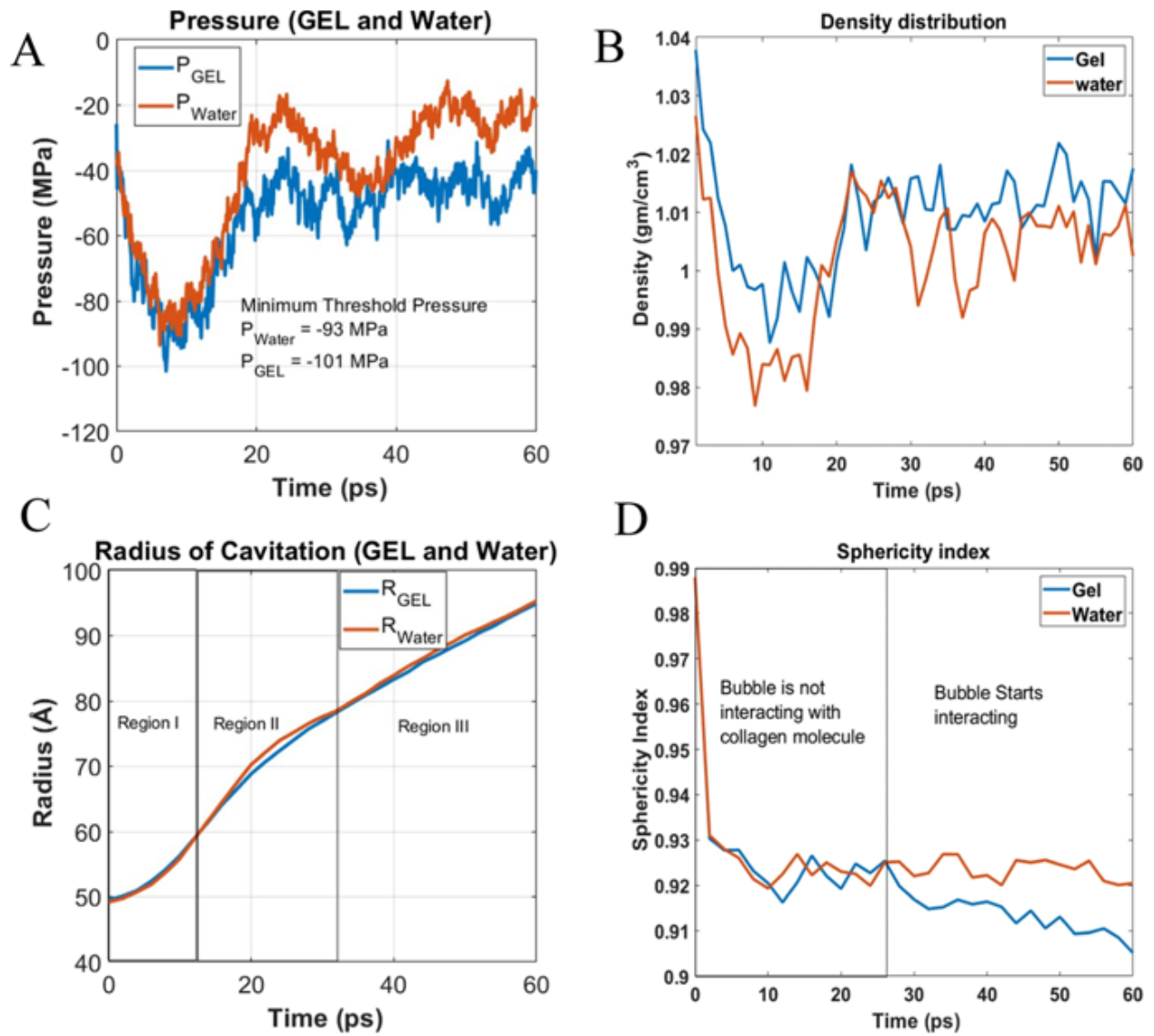
Figure 3-2 Bubble growth phenomena in water and gel like structure (A) Pressure fluctuation during cavitation growth. (B) Density variation (Exclude cavity volume during density calculation). (C) Cavitation radius (D) Cavitation sphericity index.

Table 3.1 the input values of surface tension, viscosity initial radius and density

Model	Surface tension(N/m)	Initial radius of bubble (Å)	Viscosity Pa.s x 10^{-3}	Density (g/cm^3)
Gel	0.0976	95.35	0.684	1.05
Water	0.0557	95.16	0.321	1.02
Water experimental	0.07 [63]		0.896[64]	0.99
Simulation Result from literature for TIP3P water	0.0523[65] at 300K		0.321[66] at 298K	1.002 at 298K

From the pressure plot comparison shown in Figure 3-2A, it is observed that the gel-like model requires higher negative cavitation pressure than the water only model. It has been hypothesized that there are three possible reasons for higher cavitation pressure in the gel than water. First, even though the gel network does not initially deform during the application of hydrostatic tension to the gel system, the presence of interfacial attraction between the collagen molecules and water (not present in pure water model) requires higher pressure to grow bubble in the gel system. Second, the bubble growth may require additional force for deforming the gel network. Third, surface tension and viscosity of gels may play additional roles.
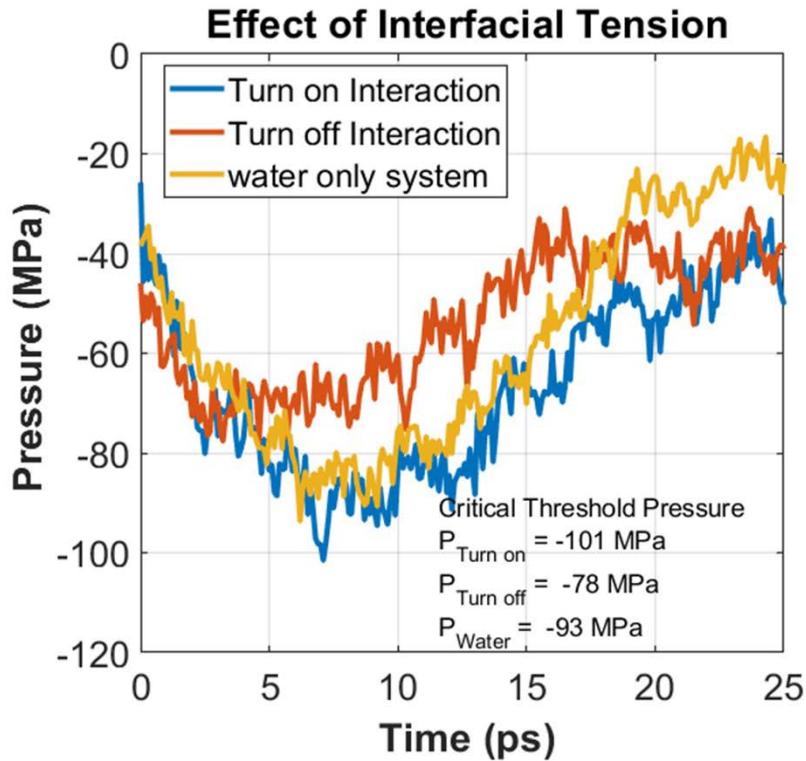
Figure 3-3 Interfacial tension between water and collagen molecules

To support the first hypothesis, an additional simulation has been conducted with the gel model

where the interfacial tension between the collagen molecules and water was turned off during the

simulation. By comparing the pressure-time relation of this model with the original gel model,

the effect of interfacial tension between the collagen molecules and water can be obtained. The

results are plotted in Figure 3-3. For a complete comparison, the pressure history of pure water is

also included in Figure 3-3. It can be observed that the critical pressure for cavitation bubble

growth in the pure water is somewhere in between the pressure for cavitation bubble growth in

the gel with active and inactive interfacial tension. In particular, the critical pressures for these

systems (water and gel in inactive interfacial potential) are recorded as -93 MPa and -78 MPa, respectively. On the other hand, when the interfacial tension is active, the critical pressure is about -101 MPa. When the interaction potential between water and collagen molecule is turned off, in principle, the interface region transforms to potential sites for cavitation nucleation. As the hydrostatic tension forces are applied, the threshold pressure goes down because of the absence of interfacial tension between water and collagen molecules. When the interfacial tension is active, the applied hydrostatic tension load is shared by the collagen network and water. It can be observed from Figure 3-4 that although deformation tension is applied to water molecules of gel, at peak pressure point (7.1 ps), the hydrostatic pressure on the collagen network reaches to minima (around -78 MPa). As such, it requires higher threshold pressure to grow bubbles in the gel system. It can be inferred from the critical pressure comparison that the interfacial tension between water and gel-network has a storng influence on the critical pressure for bubble growth.
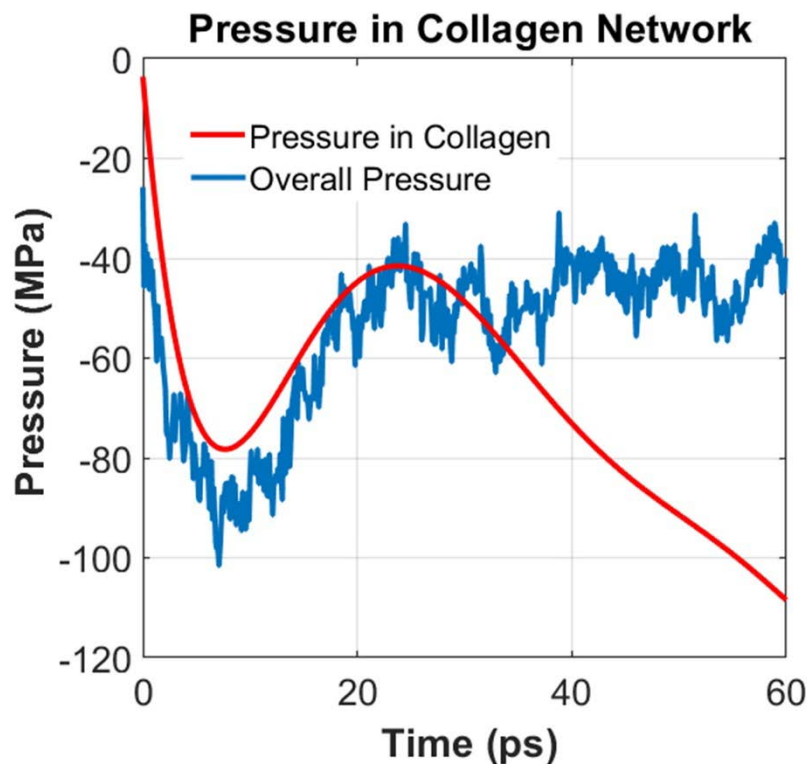
Figure 3-4 Tensile pressure in the gel network

The mechanisms of bubble growth for gel, gel without interfacial tension, and water can be visualized from the simulation trajectory. From the images, it can be observed that the bubble starts to grow uniformly and radially outward. Interestingly, the surface profiles of a bubble appear to be different from a perfect sphere. It has been argued that a bubble will retain a near-spherical shape when it grows in bulk water. Its shape will deviate from a spherical geometry when it experiences resistance from the surrounding gel network. To capture the geometric evolution of the bubble in water and gel, the real-time surface area of the simulated bubble of

radius *r* with the surface area of a spherical bubble with the same radius r is compared. This ratio is referred to as Sphericity Index Ψ. It has been calculated Ψ using the following formula[67] :

$$\Psi = \frac{\pi^{\frac{1}{3}}(6\,V_c)^{2/3}}{A_c} \qquad (3\text{-}4)$$

Where V_c is the volume of the cavity and A_c is the surface area of the cavity. For the perfect round cavitation its value is 1, when it deviates from its spherical shape the sphericity index decreases. Note that at the beginning artificial cavity is created, which is perfectly round, therefore at the beginning of deformation (0 ps) sphericity index ~1, however, when deformation starts the bubble shape sharply deviates from the perfect spherical configuration, both in gel and water. It can be observed from Figure 3-2D that the sphericity indices of bubbles in water and gel are nearly the same up until 25 ps. It implies that the bubble interacts only with the surrounding water until 25 ps. The strain energy effect of the network comes into play only after 25 ps. It can be noticed in Figure 3-2A that pressure reaches its minimum value at around 12 ps. It means, when the pressure drops to the minimum value (~12 ps), the bubble surface does not interact with the collagen molecules, as evident from Figure 3-2D. It implies that the strain energy in the form of bending, tensile, and torsion of collagen molecule is not responsible for higher cavitation pressure at this regime.

To justify the second hypothesis, we have estimated the pressure on collagen molecules only. We have found that when the bubble starts interacting with the collagen molecules (at 25 ps) to grow further, it needs to overcome the resistance arising from the deformation (predominantly

37

bending) of the gel network. It can be observed that (Figure 3-4) collagen molecules experience higher tensile pressure (negative slope) after 25 ps although the tensile pressure in the overall system is less tensile. It can be inferred that as time progresses from 25 ps and onward, the bubble growth mechanism transitions from affine to nonaffine [68] implying the network elasticity starts contributing. Form the mechanical strength correlation (Figure 3-1) at different conformation shows the elastic properties of collagen molecules at different structural conformations. It can be noticed that the stiffness of the gel-like structure is about 0.53 GPa.

To validate the effect of surface tension on cavitation pressure, the surface tension values of gel and water model are estimated. It has been found that the surface tension of the gel is about 0.097 N/m whereas the surface tension of water is 0.056 N/m. Although the reported experimental surface tension value of gelatin is less than our simulation results, it is known that the surface tension of gelatin is not a static value, rather it decreases with the gelation process[16]. The simulation of the gelation process is out of the scope of molecular dynamics study, therefore, it can be assumed that the measured surface tension is static during bubble growth and collapse process studied here. Nevertheless, the higher surface tension values in the gel system imply more pressure is required to cavitate in the gel (See Appendix A: Surface Tension Measurement). Although, the measurement of the surface tension is carried out for a perfectly flat surface, whereas the bubble surface is spherical. The approximation of the values of surface tension may induce error for the bubble growth process. Curvature depended surface tension can be calculated from the following equation[69][70]:

$$\gamma(R) = \gamma\infty(\mathbf{1} - \mathbf{2}\delta/R) \qquad\qquad (3\text{-}5)$$

Here γ_∞, is the surface tension for a flat surface and δ is the Tolman length, for different water models the Tolman length constant ranges from 0.5 Å to 1 Å [71], considering maximum length constant 1 Å for a 50Å bubble in water, surface tension $\gamma(R)$ comes out 0.055 for water, whereas for gel 0.095. Considering flat surface induces below 2% error. Therefore, in this research surface tension of a flat surface is considered for the calculation. Surface tension is one of the minor factors to affect the critical pressure as compared to other major factors such as viscosity and rigidity of the collagen molecules. It should be also noted that the morphology of the molecular systems has been studied is heterogeneous. However, the continuum theories of surface tension discussed here is based on the homogenous system. As such, these theories may not be fully applicable to this molecular system. For this reason, a direct comparison of the molecular dynamics simulation results with the theory of surface tension may not be feasible.

It is already discussed that in the gel system, the bubble starts to interact with the fibril network after 25 ps. It can be noticed from Figure 3-2D. that the sphericity index of the bubble in water and gel starts to deviate after 25 ps. It implies that the surface profile of the bubble in the gel is affected by the interaction with the gel network. Since such interaction reduces the sphericity index of the bubble in gel compared to the sphericity index of the bubble in water, a higher bubble surface area is created by the bubble in the gel than the bubble in water. This is because the surface area to volume ratio is minimum for sphere. Any reduction in the sphericity index will imply a higher surface area when the total volume is fixed. As such, additional energy is required to grow the cavitation bubble in the gel. In Wonmo Kang's work [7], the shape of a

preexisting bubble in the gel is predicted as non-spherical. In a way, our simulation at the nanoscale justifies Wonmo Kang's predictions [7] .

In summary, it can be inferred that the requirement of higher pressure in growing a cavitation bubble in the gel is primarily associated with the interfacial interactions between the gel and water and the surface tension of gel. The deformation energy of the network does not provide significant influence. However, the presence of the network affects the surface area (i.e. the sphericity index) of the bubble.

3.2.2   Pressure and cavitation radius damping

It is apparent from the Eqn ((3-1) or ((3-2) that a stable bubble will maintain its radius if pressure is maintained constant. Without losing generality, it can be inferred from these equations that small fluctuation in pressure will lead to an oscillation of bubble radii. For example, for the typical stable bubble radii commonly found in water, which varies between 1 and 100 μm, the natural frequencies are of the order, 5 to 25 kHz[72]. Knowing the frequency of oscillations of the bubble with an applied oscillatory pressure has many practical implications. As Brennen explained [72], if one plans to create cavitation in water using an acoustic pressure field, then the frequencies to most effectively generate a substantial concentration of large cavitation bubbles have to be in this frequency range. Another application where this frequency estimate is useful is in the design of cavitation damage resistant metallic turbine propellers. It is known that to test a metal's durability against severe cavitation damage, magnetostrictive devices are used to oscillate solid material samples in water (or other liquid) at these critical frequencies (kapp). Although the oscillation of the bubbles produced in this manner may be highly nonlinear, such devices can be very helpful in generating bubble clouds in the fluid.

In order to study this concept further, a study has been performed on bubble dynamics at constant system volume. From the MD simulation perspective, when the system volume is fixed and a finite temperature prevails in the system, pressure must fluctuate with time due to thermal oscillation. To simulation pressure oscillation in this system, after cavitation growth, the volume has been kept fixed and determine the pressure oscillation and the natural frequency of cavitation for both the water and gel-like models. It is quite interesting to note that pressure fluctuation in the water and gel system is similar (Figure 3-5), however presence of collagen dampens the oscillation of the bubble volume in gel-like solution.   Strasberg (1953) [73] and Morioka Mikio [74] shows that for a nonspherical bubble, it is convenient to write a differential equation of the small amplitude, a non-condensable pulsing bubble in terms of the volume pulsation v, as shown below:

$$m\frac{d^2V}{dt^2} + b\frac{dV}{dt} + kV = 0 \qquad\qquad (3\text{-}6)$$

Where, m, b, and k are inertial, dissipation, and stiffness constant. k, is proportional to inside gas pressure, in this simulation inside gas pressure is very negligible, therefore it can be omitted the third term. Constant b has four components: b_{vis} =viscous dissipation, b_{th}=thermal dissipation, b_{rad}=radiation dissipation, b_{ph}=dissipation due to liquid to vapor phase transformation. For this MD simulation study, only viscous dissipation is largely effective, since the simulation is conducted at a constant temperature thus thermal dissipation is negligible, there is no radiation, and no or negligible vapor phase inside the bubble.

$$b \cong b_{vis} = \frac{\mu}{\pi R^3} \qquad (3\text{-}7)$$

where, μ is the viscosity coefficient

The natural frequency and damping constant of the bubble are given respectively by

$$f_n = \frac{1}{2\pi}\sqrt{\frac{k}{m}}\sqrt{1 - \frac{\delta^2}{4}} \qquad (3\text{-}8)$$

$$\delta = {b} \Big/ {\sqrt{k/m}} \qquad (3\text{-}9)$$

The solution of equation (3-6)comes out:

$$R(t) = C1 \times e^{\frac{-bt}{m}} + C2 \qquad (3\text{-}10)$$
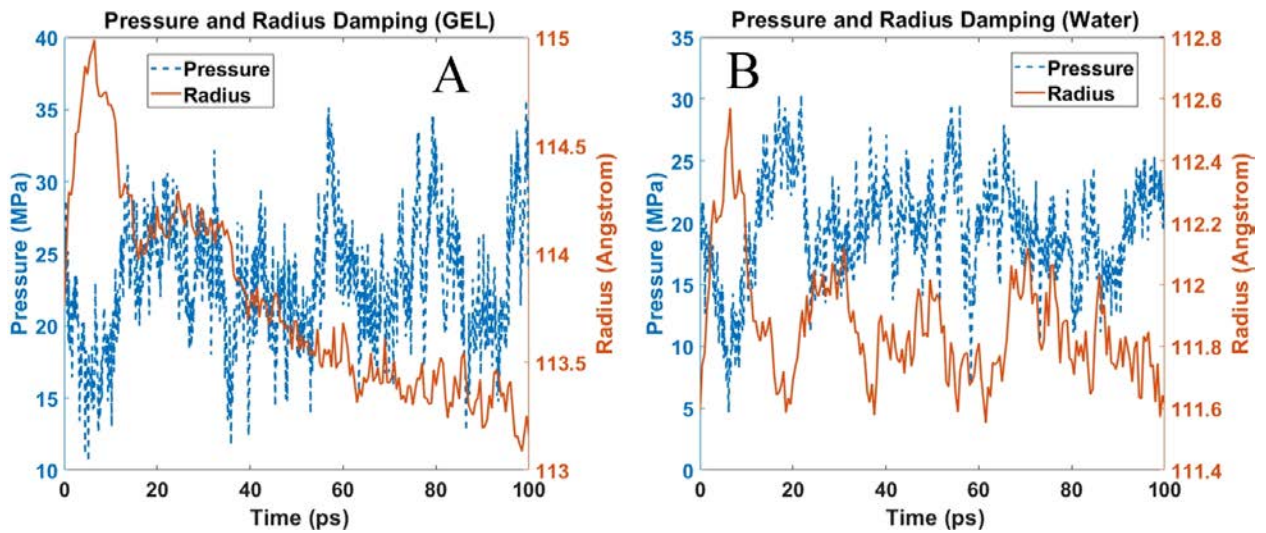
Figure 3-5 Tensile pressure in the Oscillation of pressure and radius after the growth stage at

constant volume (A) Gel, (B) Water

C1 and C2 can be calculated from the boundary and initial conditions. The measured viscosity of

the gel is almost double than water (See Appendix B: Viscosity Measurement), therefore radius

damping (Eqn (3-10)) is higher in the gel than water. The simulation results also validate the

analytical results (Figure 3-5).

A recent publication by Yonatan et al. [75] shows that 20W% Ballistic gelatin (BG) has a 25

times higher ultrasound frequency damping rate than water. However, the damping due to impact

force is not that pronounced asserting that a gel-like interconnected network structure potentially

buffers the stress field.

3.2.3   Effect of strain rate on bubble growth

The effect of strain rate on the cavitation threshold pressure is shown in *Figure 3-6*. It has been

found that bubbles at higher strain rate require additional pressure to grow. Stan et al. [12]

studied cavitation growth by imposing X-ray induced shock wave and found that decompression

time reduction from 20 ns to 2 ns reduces the cavitation pressure requirement from -30MPa to

below -100 MPa. Arvengas et al. [25] showed that at the higher acoustic frequency the cavitation

formation in water requires minimum negative pressure. This study also complies with the

experimental observation. The system volume has been expanded to grow the bubble for 60 ps

and 30 ps at X and 2X hydrostatic strain rate for the same percentage of volume expansion in

water and gel system and observed higher negative pressure required for the bubble growth at higher strain rate. *Figure 3-6* shows the result of the deformation of the gel and water system at different strain rates. It has been found that increasing the strain rate decrease the minimum threshold pressure by 26 MPa in the gel (*Figure 3-6* A). On the other hand, in the water system, it decreases 31MPa (*Figure 3-6* B). The effect of the strain rate in gel and water is quite similar. While comparing the threshold pressure of Gel and Water at 2X strain rate (*Figure 3-6* C) the difference is only 3MPa, whereas at lower strain rate the difference is 8 MPa, despite the fact of higher cavitation pressure in Gel. Moreover, some additional nucleation site is observed in the gel system at a higher strain rate. *Figure 3-7*A shows the homogenous nucleation of the bubble in gel system. Instantaneous formation of very tiny bubbles can be noticed in the gel (*Figure 3-7*A) that are absent in water (*Figure 3-7*B).

Cavitation pressure requires some time to propagate in the gel system (due to higher damping see 3.2.2) at a higher strain rate until the local pressure reached the homogenous cavitation pressure, and homogenous cavitation initiates (*Figure 3-7*). Time-lapse in the gel system is due to the viscous effect. *Figure 3-6* D shows the strain at different strain rates for both the gel and water models. Volume strain is maximum at a peak pressure for both the systems. The gel strain is higher at a higher strain rate, because the peak pressure at the localized region surpasses the homogenous nucleation threshold pressure (~150 MPa) [76] of water. Moreover, deformation is applied only in water which caused cavitation to form adjacent to gel fibril, due to higher rigidity of gel fibril it is reasonable to assume that deformation is mainly applied to the water molecules at that time scale and in this region I.
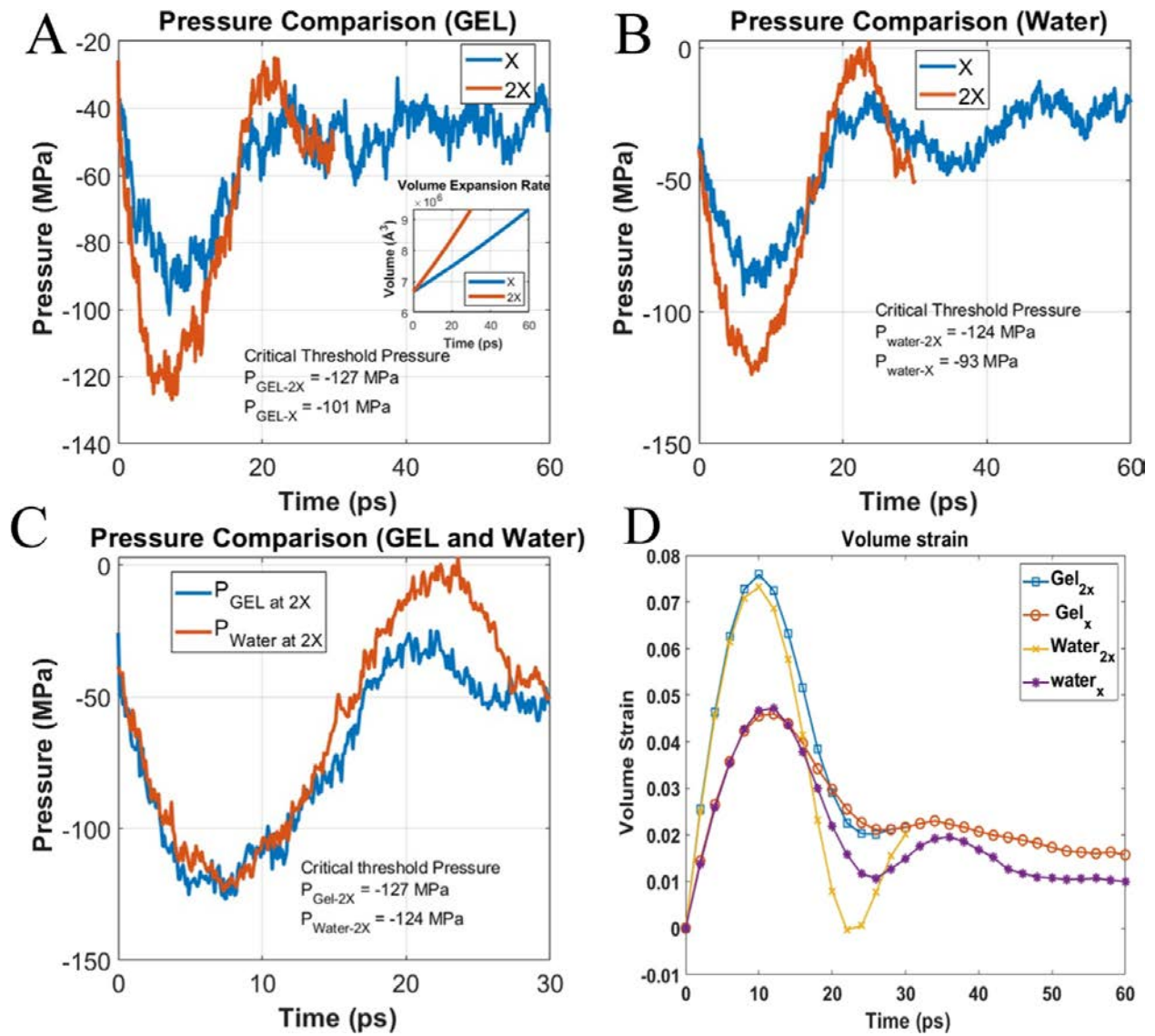
Figure 3-6 Strain rate effect on cavitation pressure (A) Cavitation pressure of gel at different strain rate (B) Cavitation pressure of water at different strain rate (C) Cavitation pressure comparison between water and gel at higher strain rate (D) Volume strain of comparison of gel and water at different strain rate. (Bubble growth at higher strain rate up to 30 ps and afterward collapse start in lower strain rate bubble grows up to 60 ps and collapse start afterward)
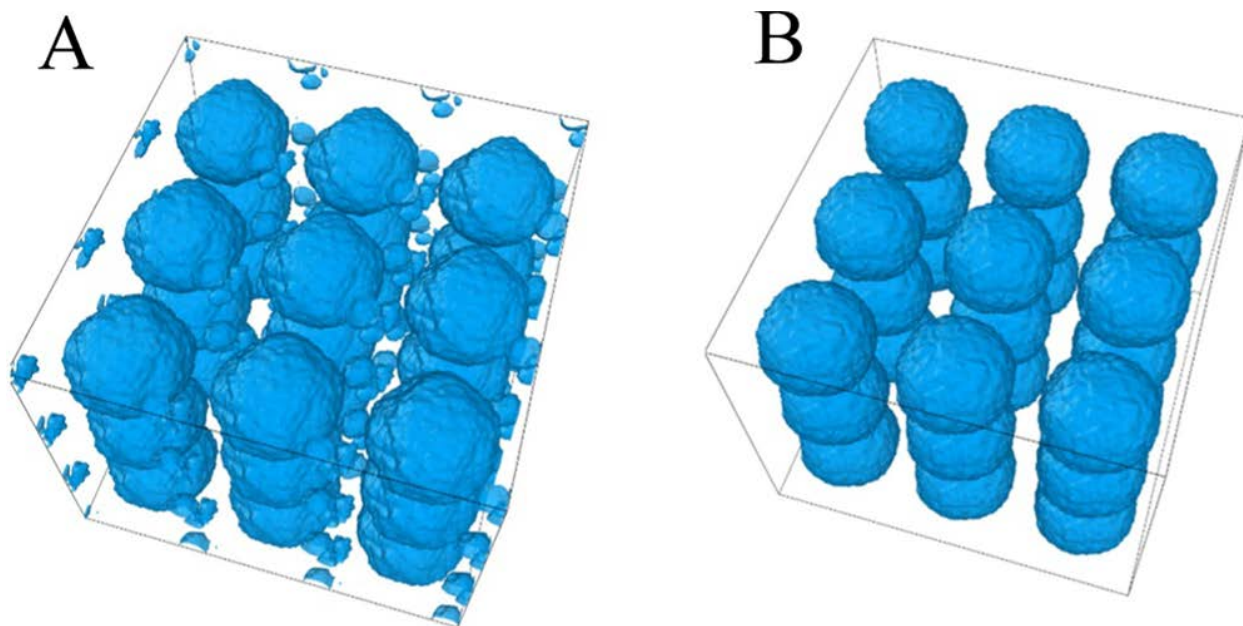
Figure 3-7 Cavitation at the end of bubble growth at a strain rate of 1.35×10^{10} s^{-1} (A) Gel, (B) Water. (For better visualization of the cavity, all the atoms are deleted from the system, 3 fold periodic image in each axis)

Minimum threshold pressure reached for water at ~6.2 ps and ~7.4 ps for X and 2X strain rates, respectively, whereas for gel it reached 7.1 ps and 7.5 ps for the corresponding strain rates. Both the systems are expanded at the same rate and the cavitation radius is almost the same at respective times (see Figure 3-2C). The delayed cavitation threshold pressure for gel at both the strain rate is due to the higher viscosity of the gel. Interestingly, at a lower strain rate of gel minimum threshold pressure reached 1ps after the water at similar dynamic condition, however at 2X strain rate critical pressure reached at the same time, which gives us the impression that at higher strain rate effect of a network is insignificant to determine the critical threshold pressure.

3.2.4 Cavitation Bubble Collapse

Here, the simulated bubble collapse mechanism has been investigated. The changes of bubble radii in gel and water with time have been recorded and plotted, as shown in *Figure 3-8*. The simulation results are also compared with the well-known Rayleigh-Plesset (RP) Equation[72], as shown in Eqn (3-11).

$$-\frac{(P_{ext}-P_b)}{\rho} = R\frac{d^2R}{dt^2} + \frac{3}{2}(\frac{dR}{dt})^2 + \frac{4\eta}{\rho R}\frac{dR}{dT} + \frac{2\sigma}{\rho R} \tag{3-11}$$

Where, R is the bubble radius, P_{ext} the pressure in the liquid, P_b the pressure inside the bubble, and ρ, η, and σ are, respectively, the density, viscosity, and surface tension of the liquid. By solving this equation, the radius vs time data is obtained and plotted (*Figure 3-8*). It can be observed that the bubble collapse time obtained from the MD simulation is different from the collapse time predicted by the RP equation. There are few reasons for such deviation. The RP equation assumes bubbles are perfectly spherical, however, it has been found that bubbles are nonspherical (Figure 3-2D). Since the stability of a nonspherical bubble is lower than a spherical one, the bubble in the MD study receives more driving force (to minimize energy) to collapse. In the RP equation, the thermal term has been ignored, the bubble surface and far-field temperature are considered constant. Besides, the liquid density, surface tension, and dynamic viscosity are considered constant [77] in the RP equation. However, based on the observation from the simulation data, density does not remain constant over time. It has been observed that (Figure 3-2B) at the peak pressure, the liquid (water) density starts to decrease from the initial density. Since the bubble is nanosized and hardly a few water molecules in vapor state can exist during collapse to put significant pressure on the bubble surface, it is reasonable to assume that P_b is negligible[11]. It has been estimated the dynamic viscosity by the Green-Kubo method (see

Appendix B: Viscosity Measurement) and the surface tension is measured following the protocol described by Bhatt et al.[65]. It can be acknowledged that the viscosity of water obtained from the simulation is significantly lower than the experimentally measured one[66]. This is possible because of the TIP3P water model is used in this simulation[66]. It is interesting to note that in the solution to the RP equation for water and gel (*Figure 3-8*), the velocity is retarded just before the collapse. At constant far-field pressure and zero vapor pressure, the RP equation has only two competing variables, the viscous term $(\frac{4\eta}{\rho R}\frac{dR}{dT})$ and the surface tension term $(\frac{2\sigma}{\rho R})$. The instantaneous velocity of the bubble is multiplied in the viscous term but it is absent in the surface tension term. Since the velocity increases with time, at some point, the viscous term starts to dominate to retard the collapse.
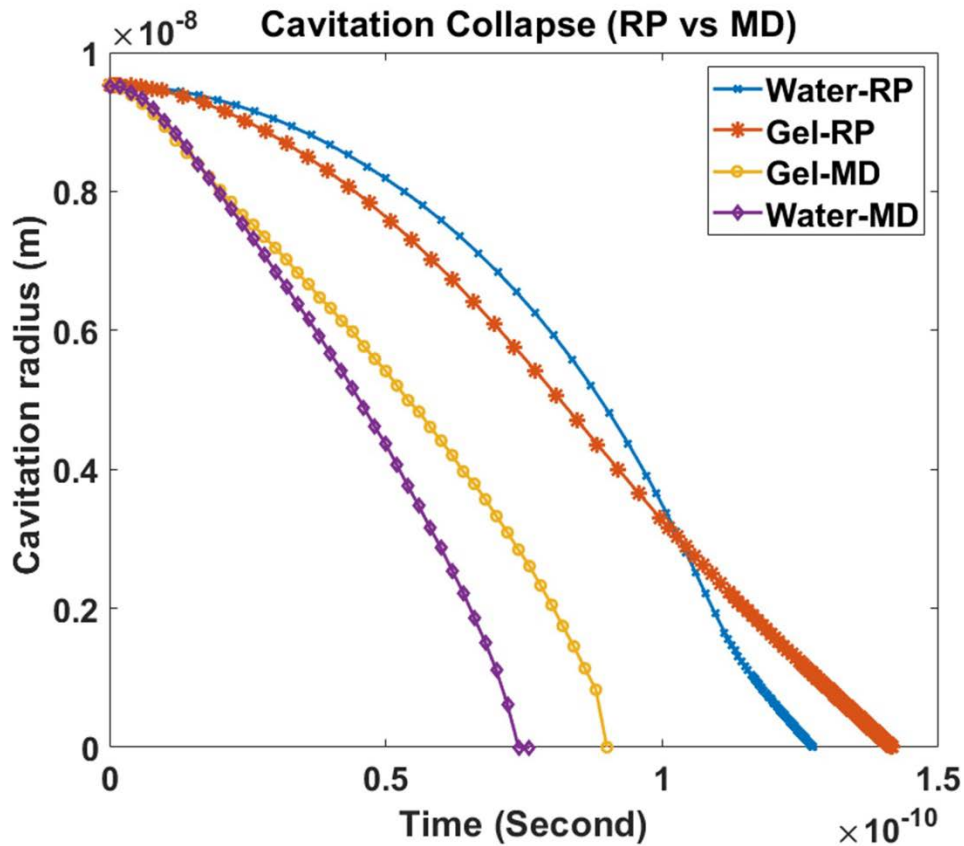
Figure 3-8 Bubble collapse time estimation from RP equation and compare with MD
result.

When the collapse time of bubbles in gel and water is compared, it can be observed that the gel

model requires more time to collapse than pure water. It can be argued that the difference in

viscosities is playing a major role in the delayed collapse in the gel system. In principle, viscosity

is inversely proportional to molecular mobility or diffusion. To compare the diffusion of

different molecules in the water and gel system, it has been estimated the Mean Square

Displacement (MSD) of gel, water, and water of the gel (excluding the collagen network) as

shown in *Figure 3-9*. For a 3D system, the diffusion coefficient is one-sixth of MSD. It can be

observed from *Figure 3-9* that the MSD of water molecule in a water system is higher than the gel system justifying the delayed collapse time of gel. Due to hygroscopic[78] nature of the collagen molecule, interfacial water is bound to hydrophilic residues of collagen molecules. For comparison, the MSD of water of the gel model is also calculated. Interestingly, in the gel model the water losses mobility due to the presence of a collagen molecule.
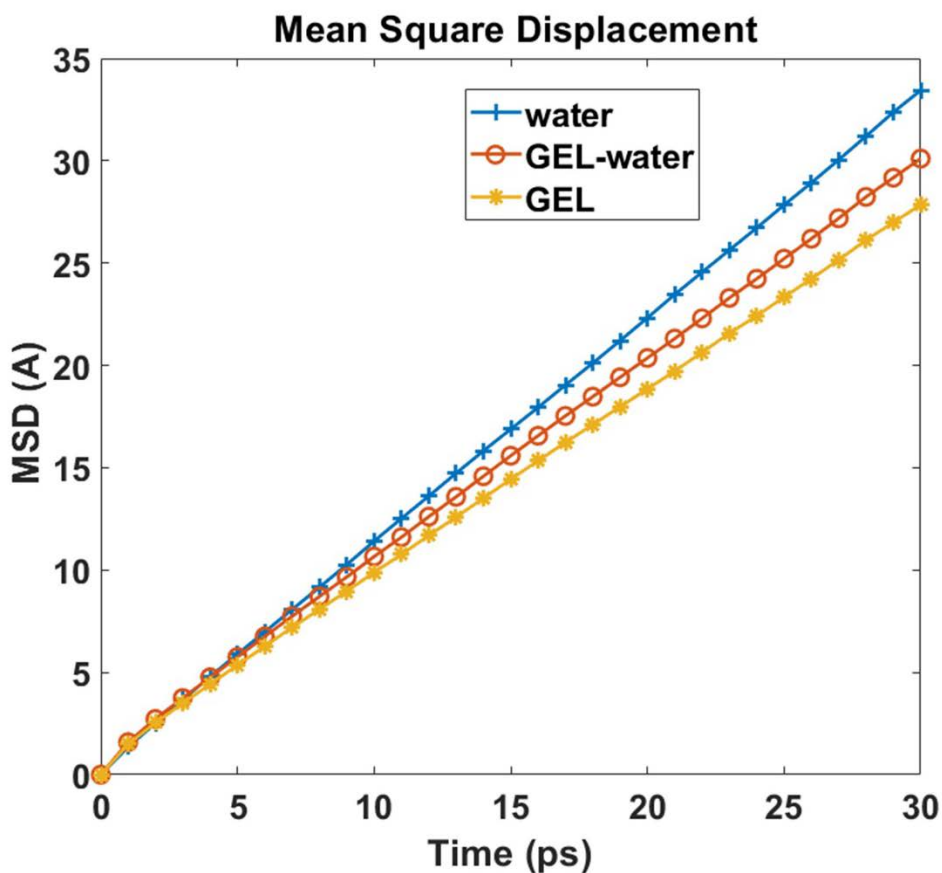
Figure 3-9 MSD of Water and gel model, for comparison MSD of water of the gel model, is also shown

3.3. Homogenous Cavitation

The Molecular dynamic simulation was carried out for both of the water and gel models (Figure 3-10) using charmm36 [51] force field in LAMMPS [56]. The size of the box is the same as the heterogeneous cavitation simulation carried out in section 3.2. TIP3P water has been used, which is best fitted with charmm36 force field potential. An incremental linear strain is applied at six different strain rates which are ranging from x=3.7 x 10^8 s^{-1} to 32x= 1.18 x 10^{10} s^{-1}, the focus of this study is to evaluate the effect of strain rate on critical cavitation stress. The simulation was carried out at constant volume and temperature (310K) using a periodic boundary condition. The simulation box was equilibrated at NPT (constant pressure, temperature, and number of the molecule) ensemble for 300 ps to minimize potential energy. After that, a constant volume rate is applied to measure the critical tensile pressure for cavitation initiation or fracture of liquid.
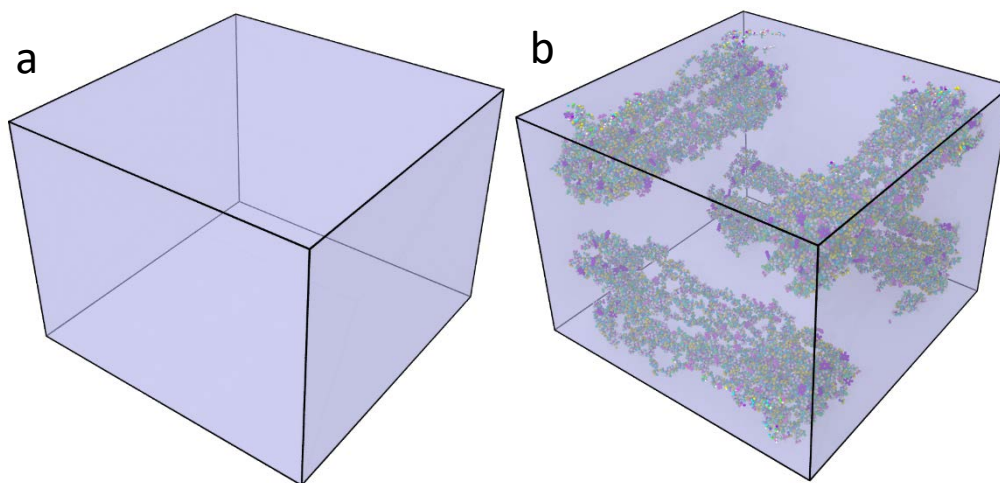
Figure 3-10 Simulation box (a) Water, (b) gel

3.3.1   Effect of Strain Rate:

It has been found that the strain rate affects the critical cavitation tensile pressure to initiate the

cavitation [79]. Researches have been conducted on critical cavitation pressure of soft materials

for a strain rate ranges from 10^{-5} $s^{-1}$to $10^8 s^{-1}$ and found that the cavitation pressure varied

from 10^5 to 10^8 Pa for a bubble size ranges from 10^{-1} to 10^5μm [79]. Critical cavitation

pressure is proportional to the surrounding pressure and inversely proportional to the radius of

the cavity [79]. However, unlike the heterogeneous cavitation strain rate has got a trivial impact

on the critical cavitation tensile pressure of homogenous cavitation [18]. During the time of

heterogeneous cavitation, the critical pressure difference is around 30 MPa for a change of strain

rate only 2 times, whereas in homogenous cavitation for a strain rate change of 32 times critical

cavitation pressure increased only 37 MPa (*Figure 3-11*). Although, it is not certain that at all the

strain rates this critical cavitation pressure change will be the same. There should have a

threshold value of critical strain rate below which strain rate has got a negligible impact on

critical cavitation pressure for cavitation formation. Figure 3-11(a, b, and c) shows that in both

the models at higher strain rate critical pressure is higher and interestingly the gel model requires

higher tensile pressure for cavitation than the water at a strain rate less than <<8x. Critical tensile

pressure for both water and gel is measured, the study found that at extremely high strain rate

critical tensile pressure is almost the same for both the models (Figure 3-11d). The apparent

discrepancies of the critical homogenous cavitation pressure between water and gel can be

explained based on the viscosity and MSD value of the two models considered. Mean Square

Displacement (MSD) as shown in *Figure 3-9* of water model and gel model (separate

displacement for gel fibril and water molecules) shows that the MSD value at the end of 30ps for

water model is 33Å, whereas for the water of the gel model it is 30Å, and for full gel model

(including gel fibril and water) 27Å. This depicts that in the gel model self-diffusion coefficient of water molecules is lower than the water of the water model, therefore we can assume that water molecules are strongly bound to the collagen molecules of GEL model. As a result, at the time of constant stretching rate, the gel system shows more stiffness than water.
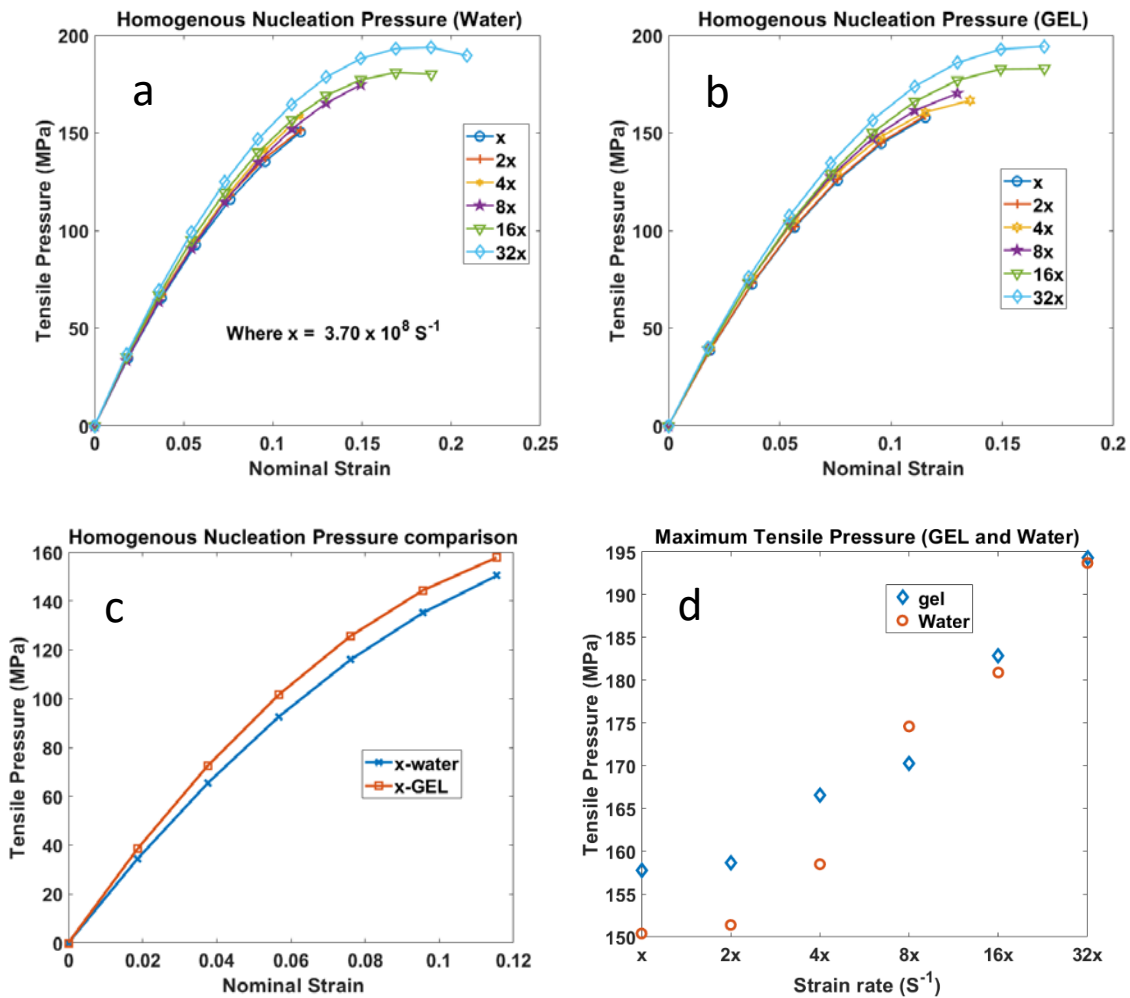
Figure 3-11 Effect of strain rates on the stress vs strain relation (a) water (b) gel (c) water and gel comparison at same strain rate (d) maximum tensile pressure of gel and water at different strain rates

Although the Gel system requires more tensile pressure at the onset of fracture to form cavitation, the volumetric strain of water is higher than gel (*Figure 3-12* a and b), the previous study [80] shows that the interfacial strength of water and collagen molecules in the gel system is strong to withstand the additional tensile pressure (Figure 3-3). Moreover, the collagen molecules which has got hydrophobic residues [81], those do not interact with water, as a result, deformation is trivial for the hydrophobic residues during the volume-controlled stretching, thus, does not contribute to the global deformation. As a result in the gel-like model, cavitation initiates at a lower volumetric strain. As the strain rate increases irrespective of the models the critical volumetric strain goes up (*Figure 3-12* b). At a higher strain rate, bubble formation rate is also higher (see section 3.3.3Nucleation rate:), therefore it can be inferred that the localized strain increased at a higher strain rate.
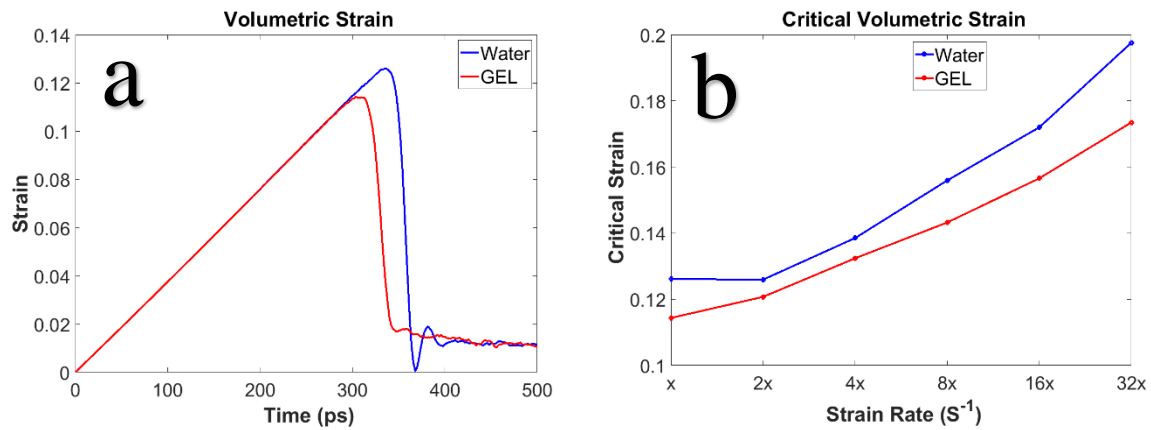
Figure 3-12 Effect of strain rates on the critical cavitation strain (a) Volumetric strain at x = 3.7 x $10^8 S^{-1}$ strain rate (b) Critical volumetric strain at different strain rates

3.3.2 Free Energy of Cavitation: Modified Formulation

Fisher [18] stated that the amount of net work w required for the reversible formation of aspherical bubble of radius r is

$$W = 4\pi r^2 \Upsilon + \frac{4}{3}\pi r^3 (P - P_o) \tag{3-12}$$

Where, Υ= surface tension, P_o is the inside pressure and p is the surrounding pressure. Bubbles in nanosize barely contain water molecule in vapor phase therefore P_o is negligible. From nucleation theory, it has been found that rate of vapor bubble formation in liquid which is subjected to negative pressure P is:

$$\frac{dn}{dt} = \frac{NKT}{h}\exp[-(\triangle f_o^* + \frac{16\pi\Upsilon^3}{3P^2})/KT] \tag{3-13}$$

Since fracture initiates when first bubble forms after t seconds, therefore it is reasonable to assume that at fracture pressure P_t, dn/dt = 1/t , where t is the fracture time. Eqn (3-13) can be solved for the fracture pressure P_t,

$$P_t = -\left[\frac{16\pi}{3} \frac{\Upsilon^3}{KT\ln\left(\frac{NKTt}{h}\right) - \triangle f_o^*}\right] \tag{3-14}$$

In Eqn (3-13)and (3-14), N= number of molecules, K= Boltzman constant, T= temperature, h= Planks constant, and $\triangle f_o^*$=free energy of activation for the motion of an individual molecule of liquid past its neighbors into or away from the bubble surface. As stated earlier, the time dependency on the first bubble formation of this quantitative equation is negligible, therefore,

fisher omitted t and free energy of activation from Eqn (3-15) to get a simplified time-independent equation to measure the fracture pressure of liquid P_l,

$$P_l = - \left[\frac{16л}{3} \frac{Y^3}{KTln\left(\frac{NKT}{h}\right)} \right]$$

(3-15)

However, this study suggests that there is an effect of strain rates on the critical fracture pressure. The MD simulation study (Figure 3-11a and d) suggests that the change of strain rate 32 times there is a 28 % increase of critical cavitation pressure for water. On the other hand for the Gel model 23.5% increase of the critical cavitation pressure is observed (Figure 3-11b and d) at a similar strain rate increase.

The molecular dynamic simulation results confirm the dependency on strain rate to the ultimate tensile pressure for both the models. Recently published work by Wang et al. [20] slightly modified the nucleation theory, they have included compressibility to the liquid undergoing tensile pressure during cavitation, according to their assumption free energy of the systems undergoing tension is equal to

$$ф = V_o U_l(\varepsilon) + 4лr^2Y$$

(3-16)

where $U_l(\varepsilon)$ is the elastic strain energy density of the liquid as a function of the volumetric strain ε. From Figure 3-11, it has been found that tensile hydrostatic pressure is nonlinear to volumetric strain, the pressure strain can easily be fitted to Eqn (3-17) to estimate the K_1 and K_2. Figure 3-11 also depicts that, at different strain rates maximum tensile pressure is different

$$\sigma = K_1 \varepsilon + K_2 \varepsilon^2 \tag{3-17}$$

Where K_1 is the linear bulk modulus and K_2 is the second-order modulus for the nonlinear behavior at relatively large strains. At T =310 K for different strain rates it has been found that different values of linear K_1 and nonlinear K_2 bulk modulus, the values are tabulated in Table 3.2. By integrating Eqn (3-17) with respect to the volumetric strain, the strain energy density function can be found as

$$U_l(\varepsilon) = \frac{1}{2} K_1 \varepsilon^2 + \frac{1}{3} K_2 \varepsilon^3 \tag{3-18}$$

Volumetric strain and nominal strain is correlated by the following equation

$$\varepsilon = \varepsilon_n - \frac{4 \pi R^3}{3 V_o} \tag{3-19}$$

Volumetric strain ε is the true strain of the solid materials where bubble volume is excluded. Before cavitation formation volumetric strain and nominal strain ε_n is the same. Free energy for cavitation in terms of nominal strain can be written as

$$\Phi = V_o U_l(\varepsilon_n) + \triangle \Phi(R, \varepsilon_n) \tag{3-20}$$

where,

$$\triangle \Phi(R, \varepsilon_n) = 4 \pi R^2 Y [1 - \frac{1}{3}\left(\varepsilon_n + \frac{K_2}{K_1}\varepsilon_n^2\right)\frac{R}{l} + \frac{2 \pi l^3}{9 V_o}\left(1 + \frac{2 K_2}{K_1}\varepsilon_n\right)\left(\frac{R}{l}\right)^4 - \tag{3-21}$$

$$\frac{16 \pi^2 l^6 K_2}{81 V_o^2 K_1}\left(\frac{R}{l}\right)^7]$$

Here, $l = \frac{Y}{K_1}$, First term on the right-hand side of Eqn (3-20) gives the free energy without cavitation, while the second term is the change of free energy with cavitation in the same total volume, the detail formulation of the second term can be found elsewhere [20]. Although Eqn

57

(3-20) considers surface tension as constant, surface tension depends on the curvature of the

cavity. For a perfectly flat surface, the surface tension is maximum and for maximum curvature

of the concave surface, the surface tension is minimum, which depicts that surface tension for a

smaller cavity is minimum [11][30]. For this present analytical solution, constant surface tension

of gel and water is considered. The protocol for surface tension calculation is stated in Appendix

A: Surface Tension Measurement. The surface tension values are taken from Table 3.1.

Table 3.2 Stiffness coefficient values of water and gel from the fitted data[1]

Stiffness	x (GPa)	2x (GPa)	4x (GPa)	8x (GPa)	16x (GPa)	32x (GPa)
K1_w	1.95	2.025	1.97	1.9	2.06	2.14
K2_w	-5.627	-6.187	-5.175	-5.268	-5.908	-5.908
K1_g	2.202	2.211	2.317	2.311	2.293	2.368
K2_g	-7.231	-7.249	-8.028	-7.706	-7.166	-7.213

The non-dimensional form of the free energy plot for both the water and gel models are shown in

*Figure 3-13*a, and *Figure 3-13*b. The critical strain is measured for the water and GEL model to

evaluate the second minima which is the zero free energy value (for R>o) at the X strain rate. At

the X strain rate, the critical nominal strain value of stable bubble formation minimum free

energy is different for water and gel. The nominal strain for the stable bubble formation is higher

---

[1] K1_w = linear stiffness coefficient of water
K2_w= nonlinear stiffness coefficient of water
K1_g = linear stiffness coefficient of gel
K2_g= nonlinear stiffness coefficient of gel

in the gel than water and the inset plot shows that as the strain rate goes up the critical nominal

strain for stable bubble formation also decreases.
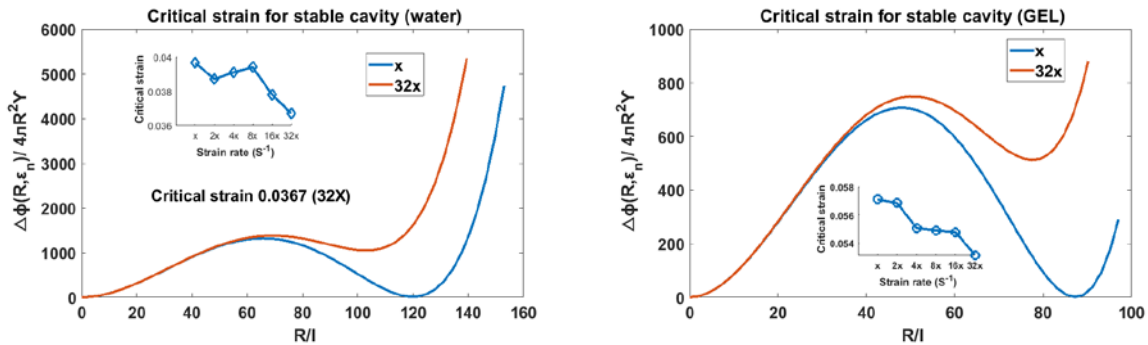
Figure 3-13 critical strain for a stable cavity concerning to free energy change (a) Water (b)

gel

The response in stress from an infinitesimal step in applied strain to an equilibrium fluid is called

stress relaxation function in rheology, the relaxation time is proportional to viscosity and

inversely proportional to temperature [82]. The gel model is more than two times viscous than

the water model, therefore the relaxation time is higher in the gel model than the water model.

This causes the critical strain for the stable cavity to go higher for the gel model than the water.

This similar logic can be implemented for a higher strain rate of each model, as shown in

Figure 3-13 a and b. at higher strain rate the critical strain for stable bubble goes down. It has

been assumed that the zero free energy point as critical strain (0.04 for water at x strain rate). At

this strain value for X strain rate reaches the zero energy minima, however, at a 32x strain rate at

the same strain value the free energy is positive, this gives us the impression of free energy

correlation at different strain rates. The inset plot of *Figure 3-13* a and b shows the critical strain

value for zero energy minima at different strain rates, although trivial change but the increasing

trend is observed. In the beginning, cavitation initiates at several points but with time the initial cavitation bubble coalescence into a single bubble. In the gel model due to the lower self-diffusion coefficient of water molecules (*Figure 3-9*), the coalescence time is higher, so the Gel solution reaches the minima at higher strain value than the water model.

3.3.3   Nucleation rate:

Wang et al. [20] stated that the nucleation rate is proportional to the strain rate or inversely proportional to the relaxation time. It is well established that at higher strain rate number of bubbles formed will be higher. The present study suggests that in the gel-like model at the critical strain point the rate of bubble formation will be higher than the water (*Figure 3-15*) (for strain rate below 2X). The hydrophobic residue of collagen molecules works as an additional nucleation site for bubble formation, therefore the probability of the number of bubble formation in the gel-like model is higher than the water model. It has been observed that the bubble formation initiates mostly near the vicinity of collagen molecules (*Figure 3-14*a point A). This visualization confirms the effect of hydrophobic surface on nucleus initiation. The points A, B, and C in *Figure 3-14*a depicts the corresponding point for fracture, maximum surface area and coalescence of multiple bubbles into the single bubble for Gel model, and D, E, F represent for water. It is quite interesting to note that the coalescence time (time difference between point E and F) for water is 26ps, whereas for gel it is (time difference between point B and C) 190ps. The difference of the coalescence time is due to the viscosity and self-diffusion coefficient of the water molecules in the Gel model. Although, surface tension plays a role to coalescence the bubble at a faster rate for the gel model than the water model, because the gel has a higher

surface tension than the water, however, at the nanoscale viscosity plays a major role on the

bubble dynamics [72].
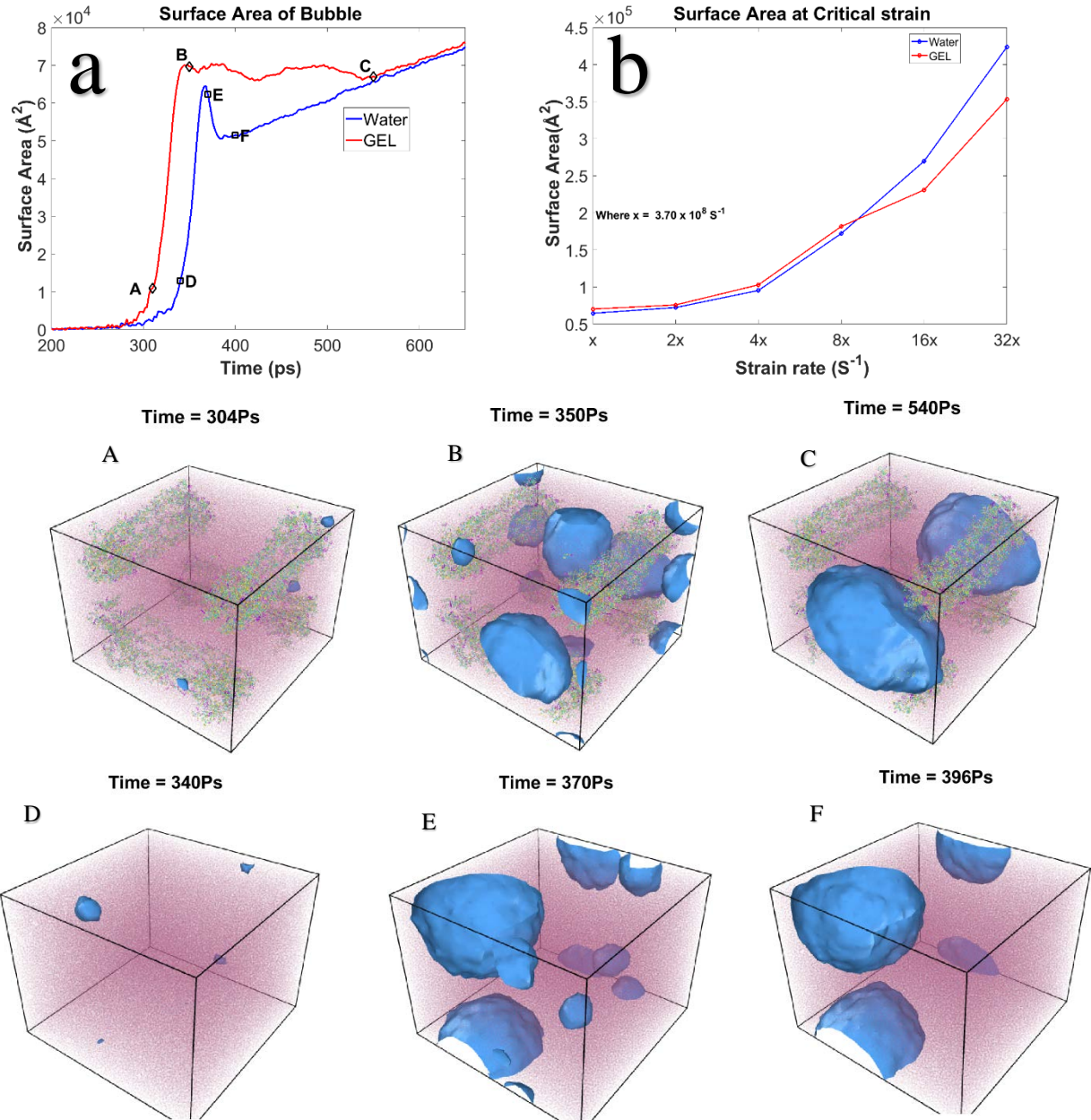
Figure 3-14 Surface area of the bubbles during the volume-controlled strain at (a) x=3.7 x 10^8 S^{-1} strain rate. Point A and D are the fracture point of GEL like and Water model respectively, Point B and E are the peak surface energy point of GEL and Water model, and point C and F are the coalescence point of the bubble of GEL and Water model (b) Surface area at the critical volumetric strain

61

Relaxation time (τ) in Eqn (3-22) is proportional to the viscosity of the medium and inversely proportional to temperature [83]. At a constant temperature, viscosity is directly correlated with the relaxation time of the medium.

$$\tau = C\frac{\eta}{T} \tag{3-22}$$

Gel solution has a higher nucleation rate than water at lower strain rate, however above 2x >> strain rate, the scenario is different (*Figure 3-15*). Nucleation rate J is defined as the number of nucleation events occurred in a unit volume per unit time, J can be correlated by the following relationship [72]

$$J_o = N(\frac{2S}{\pi m})^{\frac{1}{2}}, \quad Gb = \frac{W_{CR}}{KT}, W_{CR} = 16\pi S^3/3P^2, \text{ and } J = J_o e^{-Gb} \tag{3-23}$$

Where N is the number density of the liquid (molecules/m^3), Gb is the ratio between work required W_{CR} to form cavitation and kinetic energy (KT). Nucleation rate above 2x is no more governed by the hydrophobic nucleation site of the collagen molecules rather it is severely impacted by the number of molecules present in the system, J_o is a function of N. It is very unlikely that cavitation will grow inside the Collagen molecules, therefore number density of water molecules in the Gel model is lower than the water model. At these strain rates (2x >>), viscosity plays a critical role.
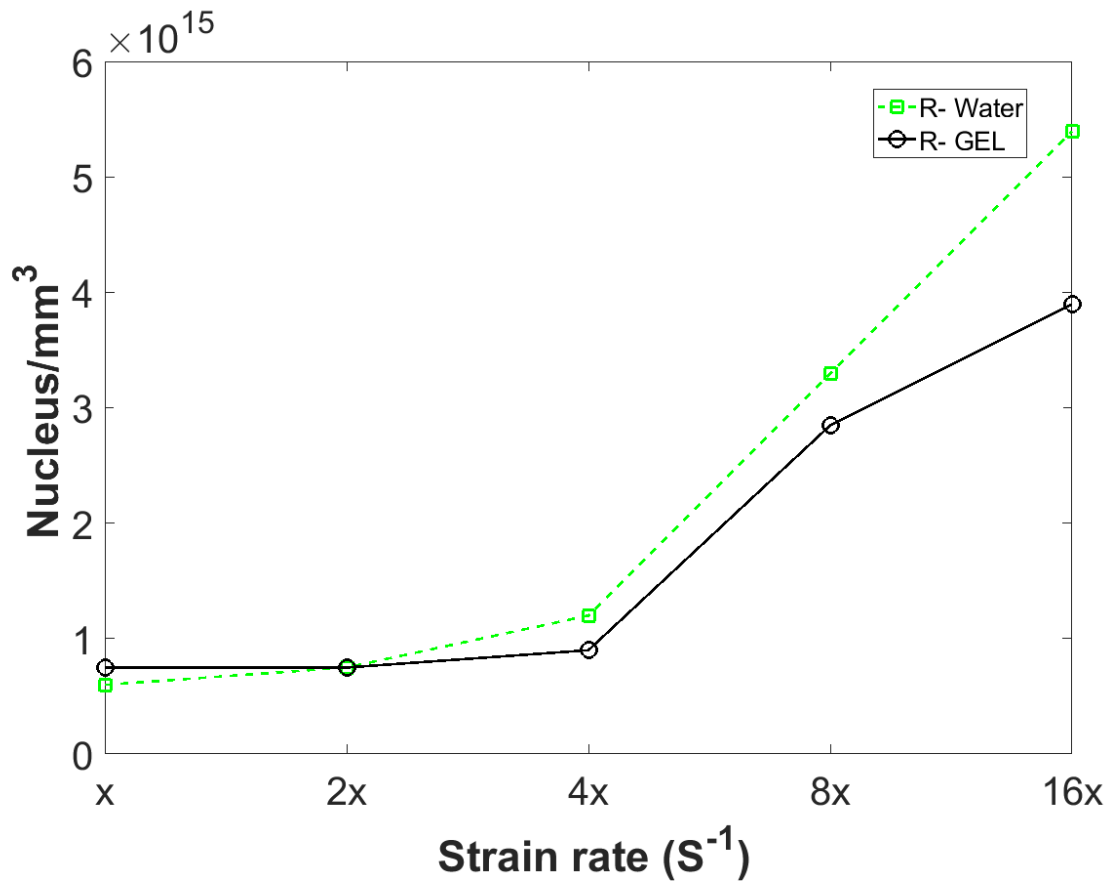
Figure 3-15 Number of nucleation site formed at the fracture point

Chapter 4:

Methodology: Shock effect on PNN

4.1. Modeling of PNN Structure

Perineuronal-net (PNN) is a protective ECM component that surrounds the neuronal cell (Figure *4-1*a). The basic building block of PNN includes Hyaluronic acid (HA), Proteoglycans (PG), Tenascin-R (TR), and Link Protein (LP) (Figure *4-1*b). Proteoglycan consists of Core Protein (CP) and Glycosaminoglycan (GAG) chains connected to the core protein via a glycosidic covalent bond. GAG chains of the CP are negatively charged, therefore these GAG side chains help to balance the charge distribution of neuronal cell. These small GAG chains have less contribution to the mechanical stiffness of the PNN, thus in this study GAG chains are omitted. In this study, the PNN structure consists of HA, TR, CP, and LP. The TR and CP are connected by non-covalent bonding, HA, and CP connected by non-covalent or glycosidic covalent bonds mediated by LP. To model the PNN structure docking protocol is used to create the most energetically favorable protein complex. For the protein-protein docking, ClusPro online server has been used [84] to perform the molecular docking. ClusPro introduced PIPER, an FFT based docking program, it uses a pairwise interaction potential as part of its scoring function E, where E is

$$E = E_{attr} + w_1 E_{rep} + w_2 E_{elec} + w_3 E_{pair} \qquad (4\text{-}1)$$

E_{attr} and E_{rep} denote the attractive and repulsive contributions to the van der Waals interaction energy E_{vdw}, E_{elec} is an electrostatic energy term, and E_{pair} represents the desolvation

contributions. The coefficients w1, w2, and w3 specify the weights of the corresponding terms and are optimally selected for different types of docking problems [85].
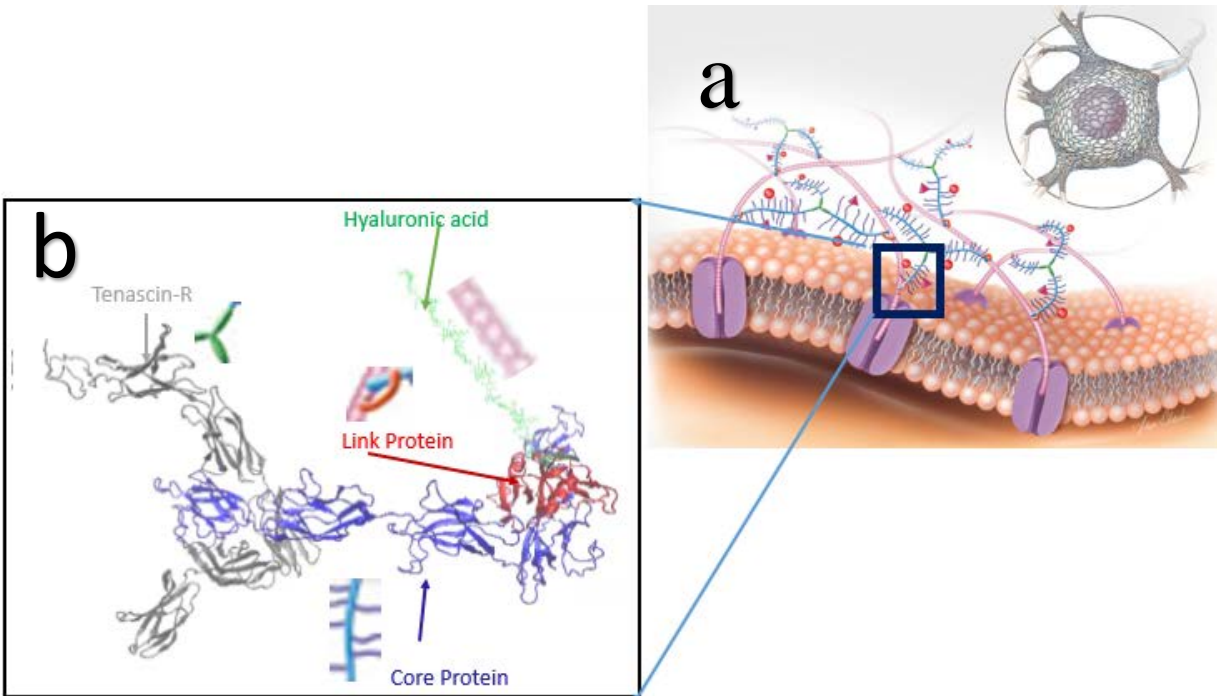
Figure 4-1 (a) Schematic illustration of PNN structure: The PNN is composed of chondroitin sulfate proteoglycans (CSPGs), which are made of a core protein (blue) flanked by several sugar chains (dark purple). CSPGs bind to hyaluronic acid (pink balls), which is secreted by membrane-bound enzymes. Link proteins (orange) stabilize the interaction between hyaluronic acid and CSPGs. Sema3A and Otx2 (pink pyramid and the red ball, respectively) bind to the sugar chains of the CSPGs. Tenascin-R (green) acts as a cross-linking protein among several CSPGs, contributing to the macromolecular assembly of the PNN [86]. (b) Docked PNN model structure

At first, LP and CP are docked, then the LP-CP protein complex is further docked with TR to get the final protein complex (LP,CP, and TR) of the PNN, finally, a hyaluronic acid chain is attached with LP by glycosidic covalent bond using CHARMM-GUI Glycan Reader and Modeler module [87]. The HA chain consists of 15 repeated dimer of β-N-Acetylglucosamine and β-D-glucuronic acid linked via alternating β-(1→4) and β-(1→3) glycosidic bonds. The PNN unit is shown in Figure 4-1b, it represents the inset portion of Figure 4-1a.

4.2. Interfacial Strength of PNN components

ClusPro server has been used for the protein-protein docking (*Figure 4-2* (B and C)) and LP-HA (*Figure 4-2* A) complex has been taken from original PDB structure of the HA binding domain of murine CD44 from RCSB protein data bank (PDBID: 2JCQ) [88]. ClusPro generated 100 energy minimized structures, only the most energy minimized configuration is taken for this study. The minimum energy configuration has been shown in *Figure 4-2* (B and C). *Figure 4-2* D shows the top 4 energy minimized structure of the CP-LP complex.
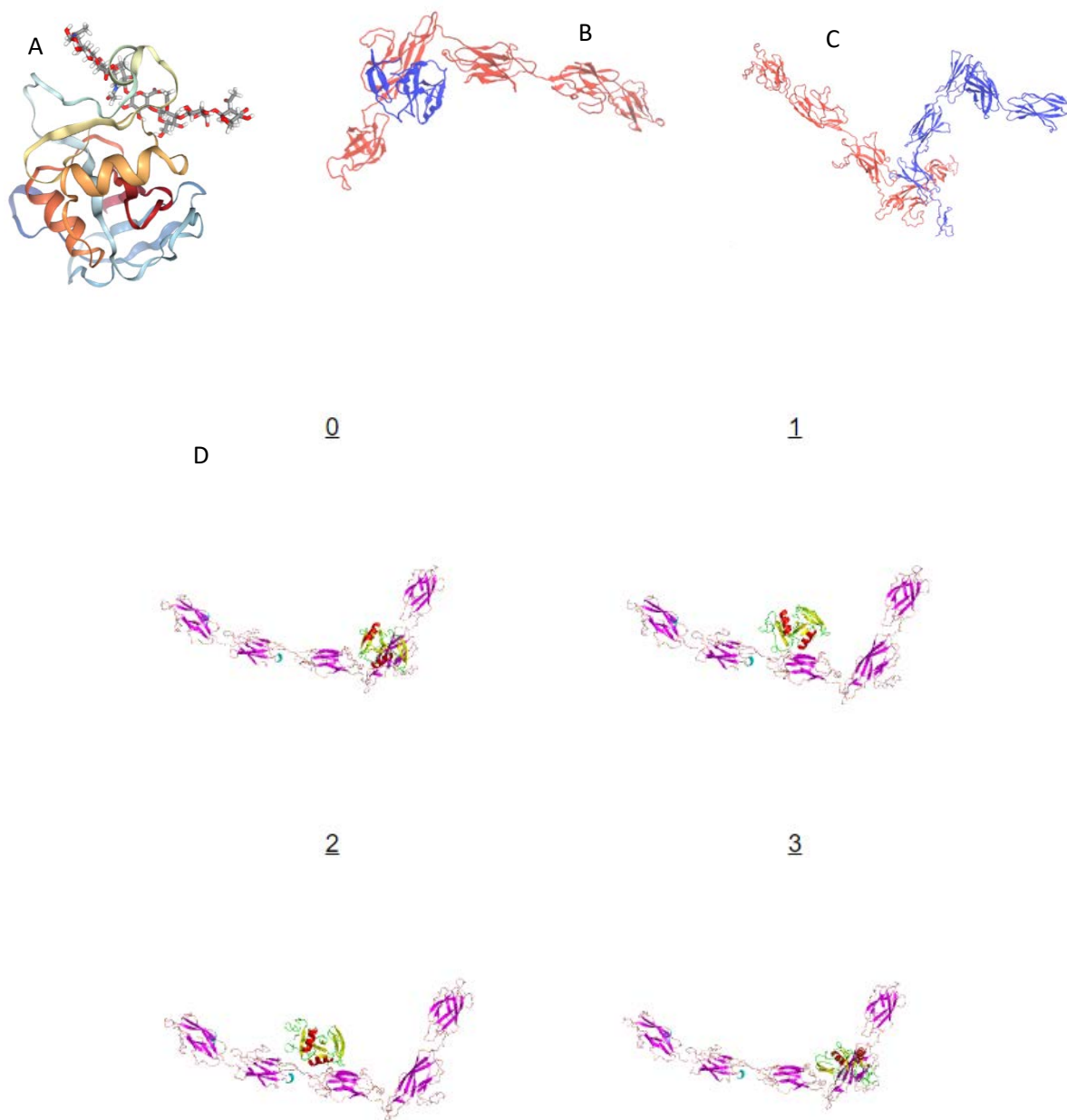
Figure 4-2 Docked Structure (A) HA-LP complex (B) LP-CP complex (blue LP and red CP) and
(C) CP-TR complex (blue TR and red CP) (D) Top 4 energy minimized structure of the LP-CP
complex

Three complex structures have been tested for the relative interfacial strength calculation using Steered Molecular Dynamic (SMD) approach in GROMACS 5.0 simulation platform [57]. The LP molecule is fixed of the LP-HA protein-ligand complex and pulled the HA at a constant speed, while for the LP-CP and CP-TR protein-protein complex, LP and TR have been pulled at a constant speed. The molecules have been pulled from their center of mass.

4.3. Mechanical property Evaluation of PNN components:

Mechanical strength of the components is important to evaluate the underlying mechanics of PNN under shock wave. Since one of the major functions of PNN is to give neuronal protection from mechanical damage, the interfacial strength of the protein complex as well as the individual strength of the components needs to be evaluated. In this study, the mechanical properties of the CP and HA have been evaluated using the CHARMM36 and ReaxFF force field. Due to the structural conformational similarity of the CP and TR, it can be assumed that the deformation profile of CP and TR will be similar. Because of the globular secondary structure, the primary covalent bond break is very unlikely for the protein molecules, rather the applied force will cause the secondary structure failure. The secondary structure of CP is globular, where each globule is connected by chain structure (*Figure 4-3*A). The whole structure contains a single chain. Whereas the HA chain contains 10 dimers.
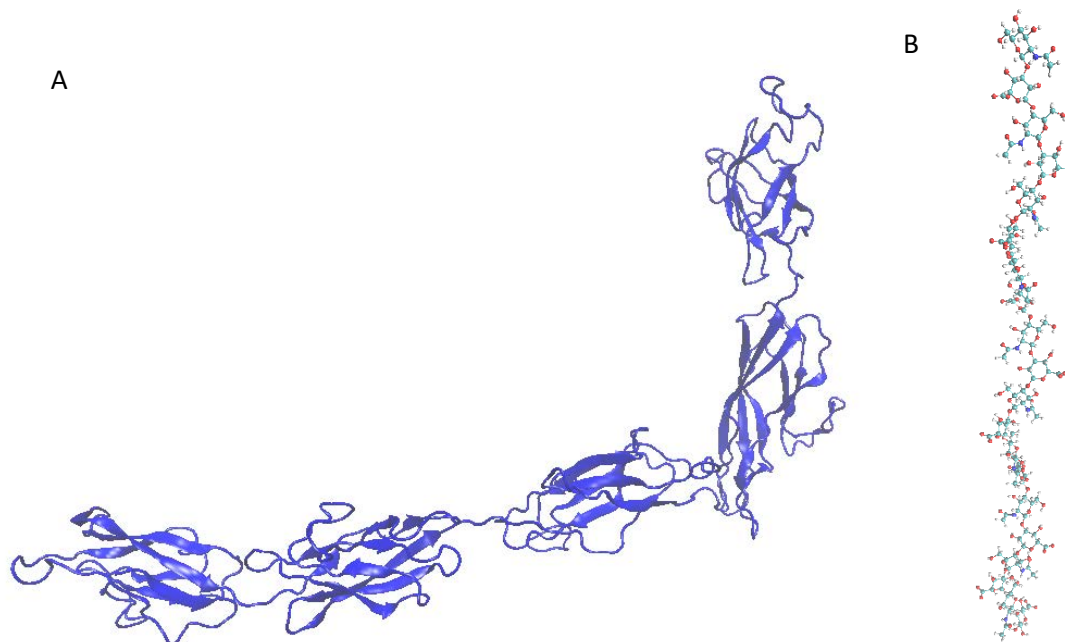
Figure 4-3 Structure of (A) CP (New cartoon) and (B) HA

Mechanical Strength of CP and HA is evaluated by the SMD approach, few atoms at the end of the molecules have been pulled at a constant velocity of 1000 ms^{-1}, while the other end was fixed at the initial position. The schematic of SMD approach is shown in *Figure 2-6*. The temperature was maintained constant at 310K in all the simulations. In the beginning, the system is energy minimized by using the shaking algorithm, after that the energy minimized structure is equilibrated at NPT ensemble, where temperature and pressure remain constant, afterward pulling simulation is conducted in NVT ensemble. In NVT volume and temperature remains constant.

4.4. Shock simulation

The PNN structure of Figure 4-1b is used to conduct the shock simulation. The PNN model is solvated with TIP3P water and ions (0.1M NaCl) using CHARMM-GUI Glycan Reader and

Modeler [87] module. The box size is $26.2 \times 26.2 \times 26.2$ nm^3, with full of water and PNN molecules. The X-direction was shock propagation direction, the shock was formed from a negative direction and allow it to propagate to the positive X direction. Both the end of X direction are opened up to create a vacuum space so that it is possible to restrict the shock flow to the opposite end because the periodic boundary condition is applied along the shock direction. There are different ways of generating shock waves, one of the most common methods is "moving piston" [89][90][91], and "reflecting boundary" is another popular method widely used [92][93][5] [88]. The piston-driven shock has several advantages over reflecting boundary, the initial number of particles in a cell remains relatively constant throughout the simulation until the shock wave nears. This gives a constant value of the density in the upstream region. Secondly, the simulation of the piston driven shock wave closely resembles the corresponding physical experiment. Even though assumptions are made on the nature of interactions among particles, and between particles and computational boundaries, the model can simulate otherwise difficult experiments [88]. To initiate the shock few layers of water molecules from the right end of the X axis are made rigid and pushed at a constant velocity for a certain distance and then the piston motion is halted. Piston are moved at a 1 km/s 2.5km/s and 4km/s velocity for 30Å distance. Density distribution of the simulation box shows that the region where PNN network molecules are present shows a 2% reduced (0.96 gm/cc) density compared to water density (0.98 gm/cc) at 310 K.
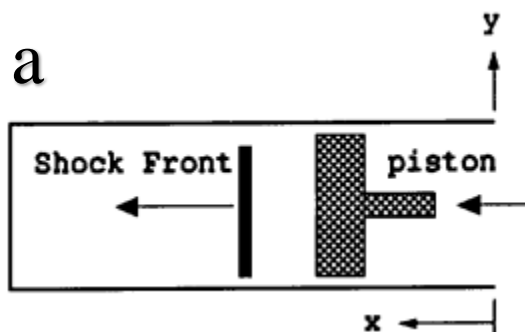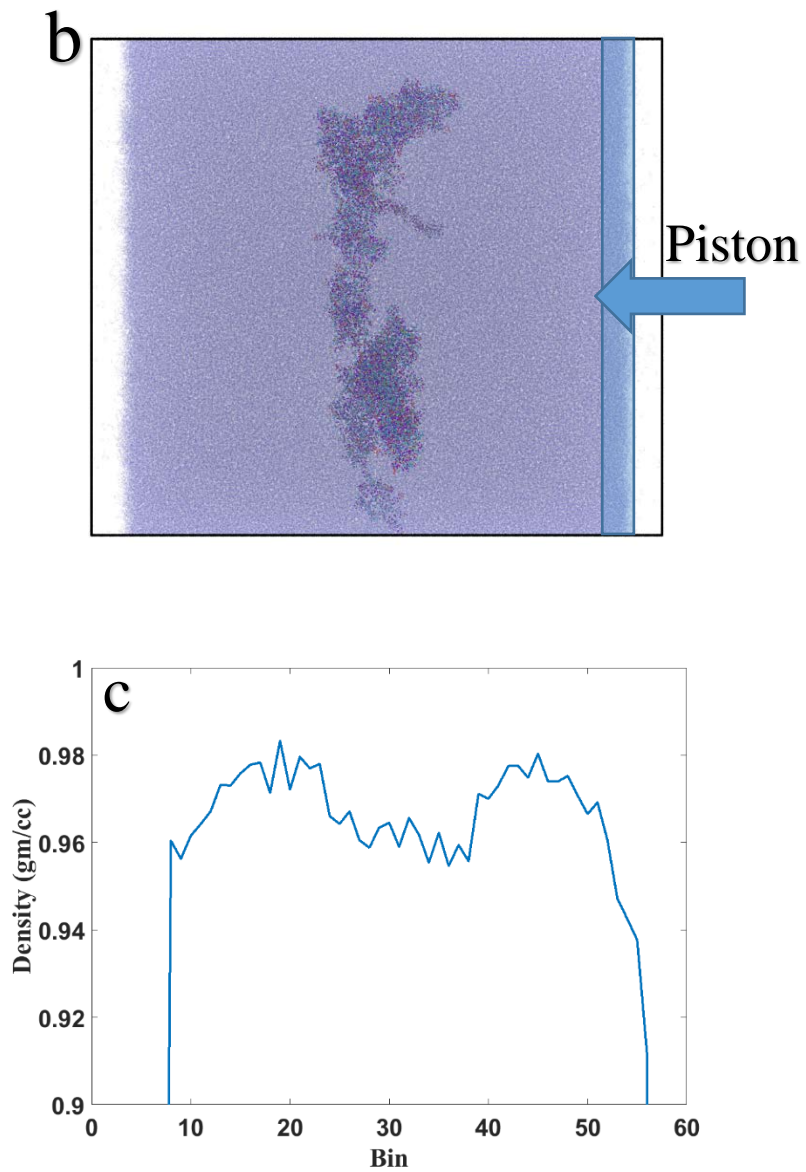
Figure 4-4 The Simulation box for shock propagation (a) Schematic illustration of the shock simulation setup [88] (b) Snapshot of the shock simulation box by Ovito visualization tool (c) Density profile along the shock direction.

Chapter 5:

Mechanics of PNN

5.1. Mechanical Strength of PNN components

Mechanical strength of the ECM components such as core protein (CP) and hyaluronic acid
(HA) is measured by SMD simulation. The CP is a very long protein coil chain which form a
secondary structure known as alpha helix and beta sheet. These secondary structures are strong
and bonded by intrachain or interchain hydrogen bond, electrostatic, and Van der Waals
interaction. During the pulling simulation the secondary structure breaks, which is mostly
noncovalent electrostatic bond. Covalent bond breakage for protein component is very rare,
therefore it is wise to use non-reactive charmm36 force field for CP. Non-reactive Charmm36
force field is advantageous over the reactive because it is widely used for biomolecules and
simulation is very fast as compared to the ReaxFF reactive force field.

In *Figure 5-1*, the CP is stretched 95% of its initial length and the maximum pulling force is only
400 pN, in contrast, the maximum pulling force for hyaluronic acid at 40% stretch is 4500 pN,
more than 10 times of the maximum CP stretched force. The HA covalent bond breaks at above
~45% strain. From the force-displacement curve of HA (*Figure 5-1*b), it can be found that at the
toe region the secondary bond stretched, and after that around 20% strain covalent bond
stretching starts and finally failed at 45% strain. The stiffness constant at the toe region is
~20pN/ Å, whereas at the covalent bond stretching region it is ~160 pN/ Å, stiffness constant is 8
times higher at the covalent bond stretching region than the toe region.
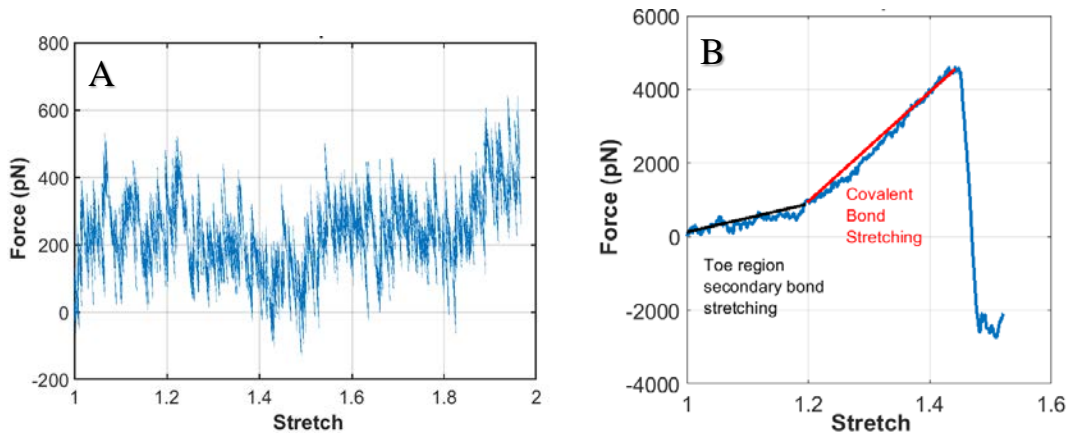
Figure 5-1 Mechanical Strength of PNN components at 1 kms^{-1} pulling speed (A) Core protein

(CP) (B) Hyaluronan (HA).

5.2. Interfacial strength:

In the PNN network, three different interfaces exist such as: CP-LP, LP-HA, and CP-TR. To

characterize the mechanics of PNN under shock wave, interfacial strength needs to be

investigated. LP, HA, and TR from the three interfaces are pulled whereas other molecules (CP,

LP, and CP) of the pairs are kept fixed at their initial position. The mass of CP>TR>LP>HA for

the PNN model. Although in reality the molecular mass of HA is maximum because of its very

long chain. *Figure 5-2* shows the relative interfacial strength of three different interfaces. It has

been found that HA-LP has the lowest strength and CP-TR is highest. The CP-TR bonds never

failed during the simulation, rather the TR molecules unfolded. The interfacial strength for the

pair of molecules considered is in between 1100 pN to 1500 pN. This strength is well below the

fracture strength of the covalent bond (see section 5.1Mechanical Strength of PNN components).

The LP-HA interface fails at around 1100 pN force, whereas the LP-CP fails at 1400 pN force.

The CP-TR did not fail during the simulation period.
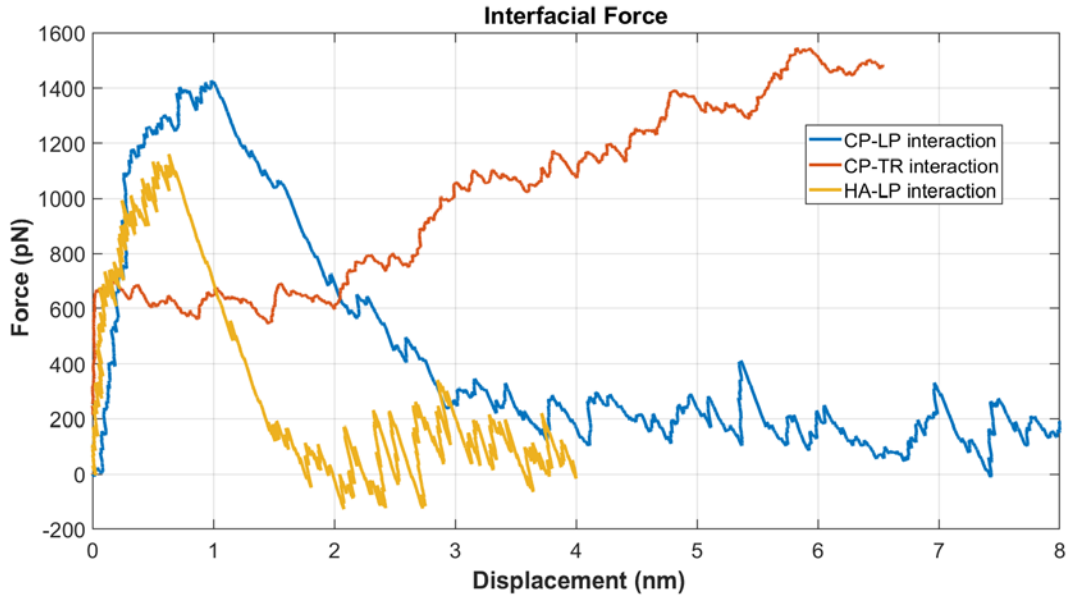
Figure 5-2 Interfacial Strength of PNN components at 1 kms^{-1} pulling speed

5.3. Shock simulation:

In this work piston is used to initiate the shock, a piston is moved up to 30 Å towards the positive

X-axis at 1 km/s, 2.5 km/s and 4km/s speed to initiate different shock speed. The inset plot of

Figure 5-3a shows the corresponding shock velocity at different piston speeds.

5.3.1   Effect of Shock Speed

As the shock starts to propagate the wavefront of the shock densified, which is the overpressure

region and after the overpressure region there is a sharp decrease of density, density profile with

time along the shock propagation direction is shown in *Figure 5-3*b. Along the shock

propagation direction, the simulation box is divided into 61 bins, each bin is 5Å in size. The

average properties such as velocity, density, and pressure are calculated for the particles in each

bin. The maximum density decays as the shock propagates, the decay rate at higher piston speed

is much higher (*Figure 5-3*a). Peak pressure at different bin locations in *Figure 5-3*c shows that

at 4 km/s piston speed maximum decay is observed and at 1km/s minimum pressure decay along

the shock direction. The decay rate at the middle (bin 25 to 30) of the simulation box is higher

for 4 km/s and 2.5km/s piston speed, however, no significant change of decay constant has been

observed for 1km/s piston speed. The presence of PNN molecules in the middle of the simulation

box may impede the motion of water molecules as the shock propagates, thus peak pressure

dropping rate is highest in this region compared to other region.   However, the penetration of

water molecules have not been hindered by the presence of PNN molecules at 1km/s, therefore

no significant change in the peak pressure observed at this region, this implies that water

molecule penetration efficiency depends on the pressure impulse, at higher pressure impulse

penetration rate is lower [39].
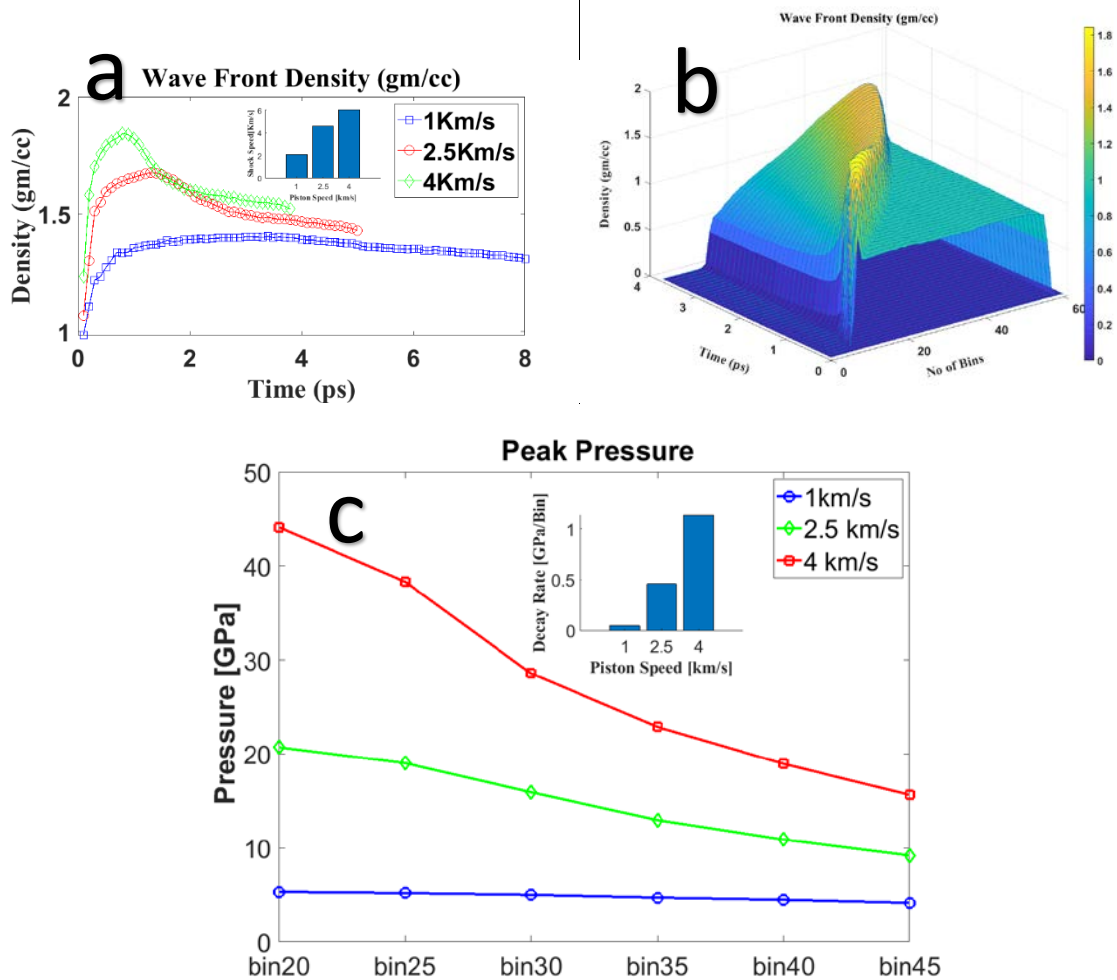
Figure 5-3 (a) Shock wavefront density at different piston speeds. The inset plot shows the corresponding shock velocity of the piston speed (b) Density distribution during the shock propagation at different location and time for 4km/s piston speed (c) Peak pressure at different bin location along z-axis during the shock propagation at different shock speed. The inset plot shows the pressure decay rate at different shock speed (each bin is 5Å along X direction)

While the shock propagates different molecules experience different levels of pressure. *Figure 5-4*a and b show the pressure profile in CP and HA, these two molecules are considered because other molecules are protein, they are representative of the structural and bonding conformation of CP molecule, therefore, it is reasonable to assume that LP and TR will experience similar pressure as CP experiences. Peak overpressure depends on the shock speed, as the shock propagates CP experience 17 GPa, 9GPa, and 3.5 GPa compressive pressure, while HA

experience 12.5 GPa, 6 GPa, and 2GPa at 4, 2.5 and 1 Km/s piston speed. It is quite interesting

to note that at almost every cases CP does not experience any tensile stress, while HA

experiences tensile pressure of around -5GPa, -3GPa, and -1GPa. This study does not confirm if

HA will break or not, however, it is reasonable to approximate the cross-sectional area of HA

around 50 to 100 Å^2 failure stress will be around 9 GPa to 4.5GPa. This value corresponds to the

breaking force of HA of *Figure 5-1*b. The approximate value of fracture stress suggests that at

4Km/s piston speed which corresponds to 6km/s shock speed HA will most likely break. The

fact that here average pressure of all atoms of HA molecule is considered, there is a possibility

that localized pressure will surpass the fracture stress at rigid junction even at lower shock speed.
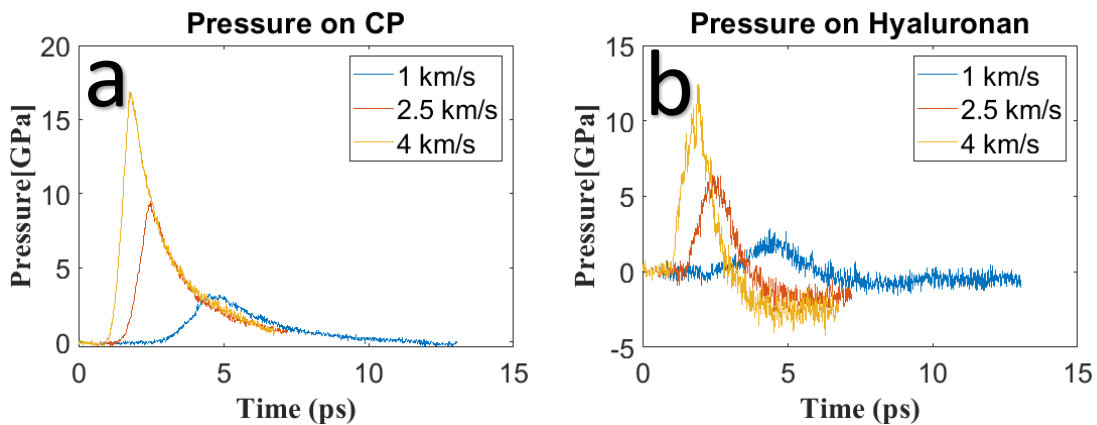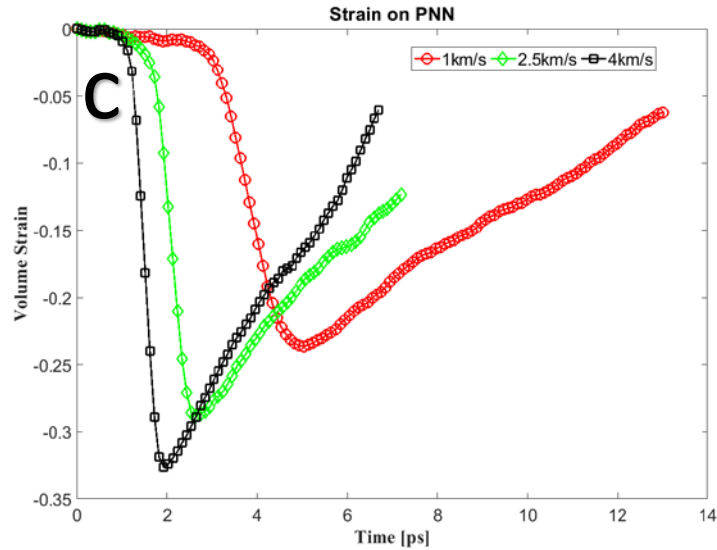
Figure 5-4 Pressure on PNN components at different piston speed (a) Pressure on Core Protein (CP)(b) Pressure on Hyaluronan (HA) (c) Volumetric Strain on PNN at different shock speed.

5.3.2 Effect of bubble

There are lot of research work that has been conducted on the effect of the bubble on the damage mechanics of biomolecules [5][94][92]. The collapse of the bubble can be symmetric or asymmetric depending on the ratio of collapsing time t_c and shock passing time t_{sp}, if the ration $(\frac{t_c}{t_{sp}})$ is higher than 1 the bubble will collapse symmetrically, otherwise asymmetric collapse will initiate. The ratio is related to the bulk modulus (B_L) and peak pressure difference ($\triangle p$) (Eqn ((5-1)). The bulk modulus of water is around 2.2 GPa, which means the cavitation bubble in water can only be asymmetrically collapsed by a shockwave having more than 2.2 GPa post-shock pressure or near that scale[92].

$$\frac{t_c}{t_{sp}} = \sqrt{\frac{B_L}{\triangle p}} \qquad (5\text{-}1)$$

In this case, the peak pressure is way higher than 2.2 GPa, therefore it is reasonable to assume that the bubble will collapse asymmetrically. The asymmetric collapse of the bubbles forms water-jet that can reach further away from the cavitation epicenter and can cause more damage. It has been investigated the pressure profile of the PNN components in the presence of a bubble of 8nm diameter and found an insignificant change of overpressure (*Figure 5-5*). However, the overpressure on the bubble projected zone of the CP molecule is higher than the without bubble model for 4km/s piston speed (*Figure 5-5*b). The portion of the CP molecule on the bubble projected zone is shown in *Figure 5-5*c.
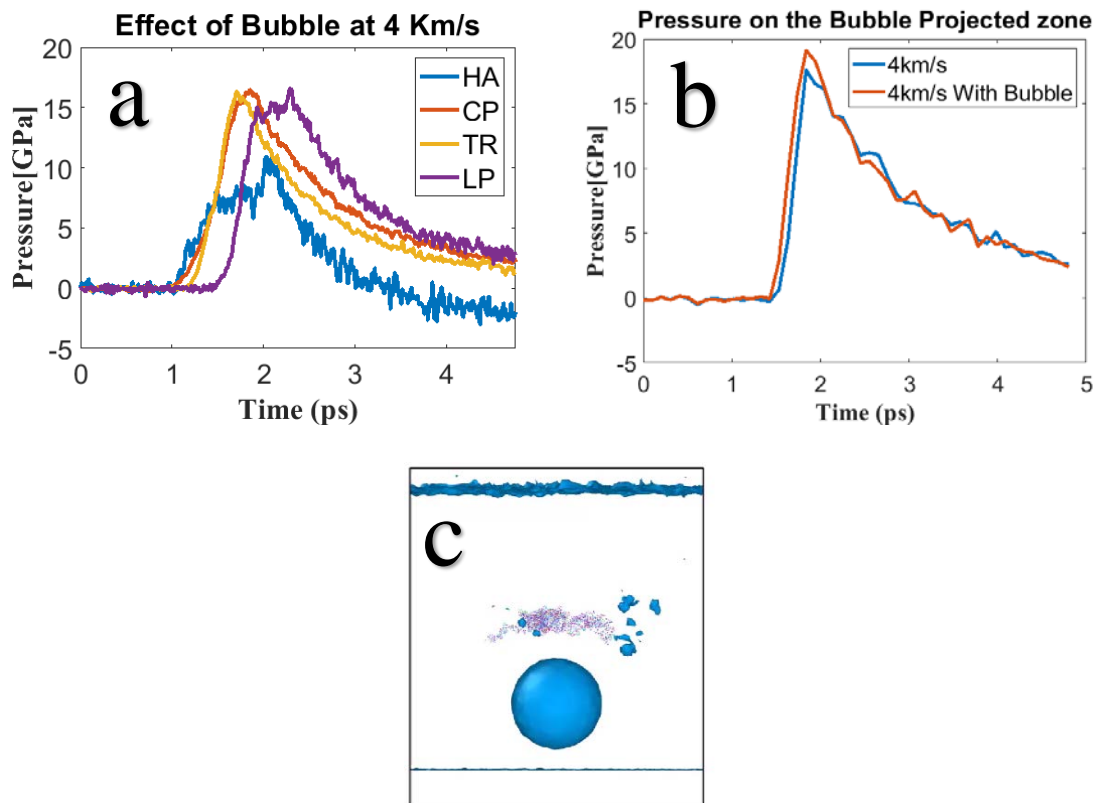
Figure 5-5 Bubble induced shock propagation (a) Pressure on different PNN components (b) Pressure on Bubble projected area (c) bubble projected area of the PNN

It is quite interesting to note that although the maximum average overpressure of the components falls in presence of bubble, the projected overpressure increases, which gives us the impression that the presence of bubble enhances the localized damage.

5.3.3   Effect of boundary condition

The PNN components are interlinked by covalent and non-covalent (electrostatic and Van der Waals bonding). There will be a difference in the acceleration profile of the components, therefore it is reasonable to assume that one part of the molecule may experience 15 GPa, while other parts still at the atmospheric pressure. The links are often considered rigid as compared to

the molecule itself. It has been observed that only HA molecule experience negative tensile pressure due to fixing one end. Although two atoms at the two end of TR are fixed, the average pressure of TR does not change significantly (*Figure 5-6*a and b). HA mostly experiences tensile pressure due to its chain conformation, the proteins are globular structure. It has been found that the fixed end of HA experienced higher tensile pressure than the middle portion and the portion connected to the LP (*Figure 5-6*c).

Finally, number of hydrogen bonds has been measured at different conditions (*Figure 5-7*), as the shock speed is increasing the number of hydrogen bond severely impaired, a hydrogen bond is only found in the protein molecules. This suggests that the secondary structure of the protein impaired due to the shock wave. The lowest number of a hydrogen bond is found for the model with the preexisting bubble, which suggests that bubble jet causes maximum damage of the PNN.
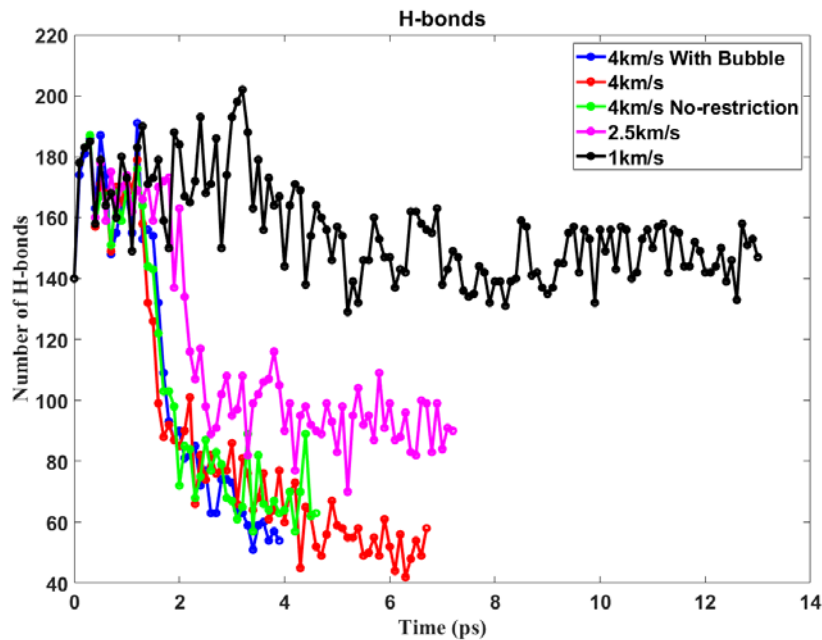
Figure 5-7 Number of Hydrogen bonds at a different speed and boundary condition (cut off distance 3Å and angle 20⁰)

Chapter 6:

Conclusions and Future Work

6.1 Summary and Conclusions:

6.1.1   Heterogeneous cavitation:

The nanobubble growth and collapse mechanism in pure water and gel model have been studied. Due to computation limitation, the radius of the bubble is limited to 5 nm only. The following conclusions can be drawn from this study:

- The results suggest that the cavitation bubble requires higher pressure to grow in the gel solution. The additional pressure is associated with the energies to overcome interfacial tension of water and gel, bending stiffness of gel-like fibril, and surface tension of the solution.

- At higher strain rates, the gel-like structure invokes homogenous nucleation despite the presence of a large bubble, which suggests that the pressure propagation rate in the gel is lower than that in water. In other words, the presence of gel microfibril facilitates homogenous nucleation.

- Cavitation collapse time is dominated by the viscosity of the medium. Surface tension plays an insignificant role.

Thermodynamics of bubble growth needs detailed analysis from the free energy perspective. Quantification of cohesive force between gel fibril and water and strain energy absorption by

fibril may give an insight into the correlation between threshold pressure difference of water and gel system during bubble growth. A detailed study will appear in future work.

6.1.2   Homogenous cavitation:

While heterogeneous cavitation critical pressure is strongly influenced by the strain rate and interfacial tension of collagen and water, the homogenous cavitation shows the trivial effect, therefore the underlying mechanism of homogenous and heterogeneous cavitation is different. The following conclusions can be drawn from the homogenous cavitation study:

- The critical cavitation pressure of gel-like model is higher than the water model at lower strain rate, however, at an extremely higher strain rate the cavitation pressure is similar for both the models.

- The modified nucleation theory suggests that the critical strain for the free energy minima is higher for the gel-like model than the water, and as the strain rate increases the critical strain decreases. The higher coalescence time of the nucleation initiation bubbles makes the critical strain for free energy minima higher for gel-like model.

- The viscosity of the models plays a critical role in controlling the number of nucleus formation, critical cavitation pressure, and nucleus coalescence. The MSD value of water is governed by the viscosity of the medium and interfacial cohesive force between the water and collagen molecules.

Lots of work have been conducted to evaluate the cavitation mechanism of water. Cavitation nucleation is well understood for water, however, the mechanics and apparent discrepancies of homogeneous cavitation pressure of Gel-like soft materials are not well revealed by the scientific

community. This ongoing effort is made to understand the underlying mechanics of homogenous cavitation of soft materials.

6.1.3   Mechanics of PNN under shock wave:

The PNN network protects the neuron from physical damage, reduces the oxidative stress, and conserve charge balance to facilitate neurotransmission. Therefore, the damage probability of PNN under shock loading needs to be evaluated. From the shock loading simulation, it can be concluded that:

- The protein structure is less prone to failure due to shock loading, while hyaluronan is the most vulnerable molecule to break during the shock loading.
- The damage efficiency is strongly dependent on the shock speed, presence of bubble, and boundary condition. Presence of bubble in the system initiates asymmetric collapse during shock propagation and exerts water jets to damage the molecules which are present in the projected domain.
- Although the pressure on the protein components is still compressive, the significant reduction of the number of hydrogen bond of the proteins makes it clear that at a higher shock speed secondary structure of the protein altered.

Although PNN does not function on carrying the action potential from one neuron to another, the presence of it is essential for the process to initiate. The absence of PNN may cause severe disruption of neurotransmission at the synaptic cleft.

6.2 Future scope

6.2.1 Continuum scale cavitation mechanics:

- Perform SEM/FIB imaging of the freeze-dried sample

- Create a 3D mesh out of the gelatin SEM/FIB stack of images

- Analysis of the cavitation phenomena using FEA Fluid-structure interaction method in macroscale
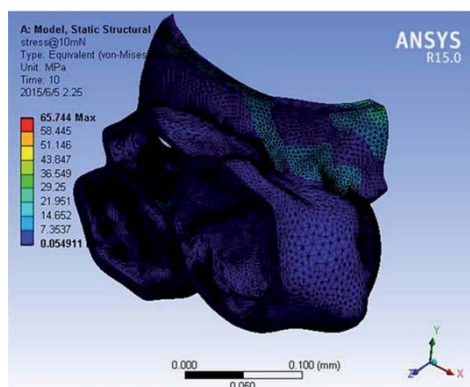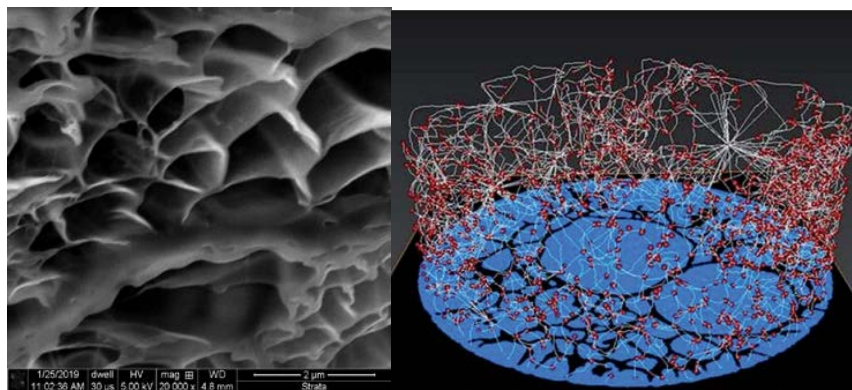
Figure 6-1 (A) SEM-FIB image of gelatin   (B) schematic of 3D reconstructed image hydrogel

[95] (C)   3D Mesh of hydrogel [95]

Appendix

Appendix A: Surface Tension Measurement

We have measured the surface tension following the protocol stated by Vega el at. [96]. Our box

size is $211 \times 211 \times 165$. Open surface is created in the z direction. For a subcritical temperature,

this setup is expected to stabilize two planar vapor-liquid interfaces perpendicular to the z axis of

the simulation cell. Molecular dynamics simulations are performed using LAMMPS to generate

the molecular trajectories using a time step of 1 fs. The temperature was kept constant by using a

Nose-Hoover thermostat with a damping constant of 1 ps. The inhomogeneous system is first

allowed to equilibrate over 300 ps, and running averages are then collected over an additional

run of around 1.5 ns depending on the thermodynamic conditions. The LJ part of the potential is

truncated at 8 Å and a switching function is used between 8 and 10 Å. Long range columbic

potential is calculated using pppm (particle-particle particle-mesh) solver, which maps atom

charge to a 3d mesh, uses 3d FFTs to solve Poisson's equation on the mesh, then interpolates

electric fields on the mesh points back to the atoms. The diagonal component of pressure is used

to measure the surface tension. Here normal component of pressure is Pzz, whereas tangential

component of pressure is arithmetic mean of Pxx and Pyy.

Surface tension, $\gamma = \int_{\infty}^{\infty} dz \ (P_N(Z) - P_T(Z))$

Where,

$P_N (Z)$ = Normal components of pressure tensor,

$P_T (Z)$ = Tangential components of pressure tensor
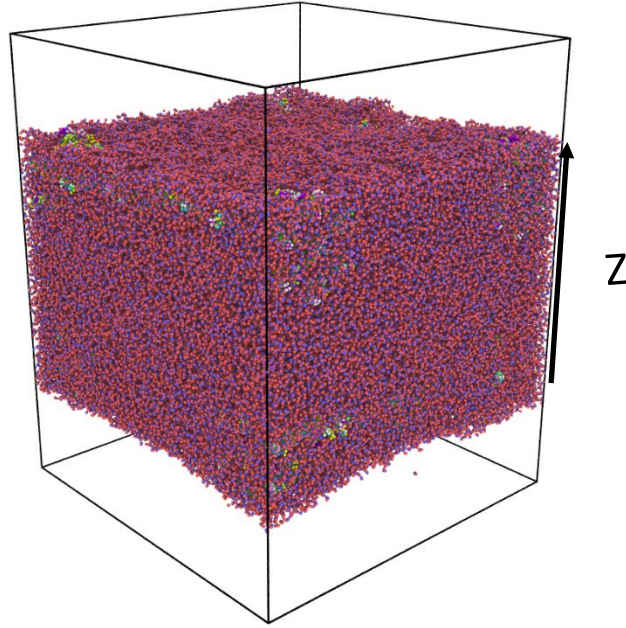
Figure 1-0-1 simulation box for surface tension measurement

Appendix B: Viscosity Measurement

We have measured dynamic viscosity by Green Kubo technique [97] of gel like structure and

water in LAMMPS. The detail scripting of viscosity measurement is stated in LAMMPS [56].

We have solved the following equation for viscosity measurement. We have used NVT ensemble

for viscosity calculation, where temperature was fixed at 310K with a damping constant 1ps. To

get appropriate viscosity value simulation was run for 100 ps. LJ cut off was fixed at 8 Å and

outer cutoff was 10 Å. Electrostatic force was calculated using PPPM technique. Figure 2 shows

the initial simulation box of viscosity calculation, where box size 211 Å × 211 Å × 165Å.

Dynamic viscosity, $\eta = \frac{V}{k_B T} \int_0^\infty dt\, (P_{xy}(0)P_{xy}(t))$

Where,

V= volume of the particle system

T= is a temperature, 310K

k_B= Boltzmann constant

P_{xy}= off-diagonal element of the stress tensor
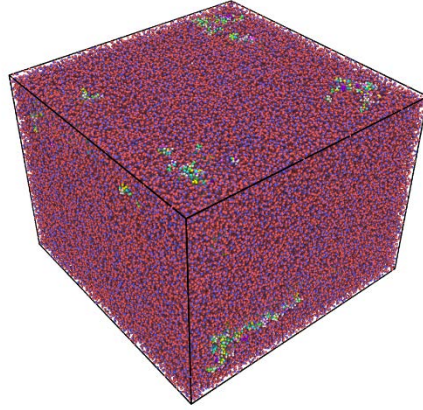
Figure 2-0-2 Simulation box for dynamic viscosity measurement

References:

[1] K. H. Taber, D. L. Warden, and R. A. Hurley, "Blast-related traumatic brain injury: what is known?," *J. Neuropsychiatry Clin. Neurosci.*, vol. 18, no. 2, pp. 141–145, 2006.

[2] J. Goeller, A. Wardlaw, D. Treichler, J. O'Bruba, and G. Weiss, "Investigation of cavitation as a possible damage mechanism in blast-induced traumatic brain injury," *J. Neurotrauma*, vol. 29, no. 10, pp. 1970–1981, 2012.

[3] A. Nakagawa *et al.*, "Mechanisms of primary blast-induced traumatic brain injury: insights from shock-wave research," *J. Neurotrauma*, vol. 28, no. 6, pp. 1101–1119, 2011.

[4] Y.-T. Wu and A. Adnan, "Damage and Failure of Axonal Microtubule under Extreme High Strain Rate: An In-Silico Molecular Dynamics Study," *Sci. Rep.*, vol. 8, no. 1, p. 12260, 2018.

[5] Y.-T. Wu and A. Adnan, "Effect of shock-induced cavitation bubble collapse on the damage in the simulated perineuronal net of the brain," *Sci. Rep.*, vol. 7, no. 1, p. 5323, 2017.

[6] A. E. Forte, S. Galvan, F. Manieri, F. Rodriguez y Baena, and D. Dini, "A composite hydrogel for brain tissue phantoms," *Mater. Des.*, vol. 112, pp. 227–238, Dec. 2016.

[7] W. Kang, A. Adnan, T. O'Shaughnessy, and A. Bagchi, "Cavitation nucleation in gelatin: Experiment and mechanism," *Acta Biomater.*, vol. 67, pp. 295–306, Feb. 2018.

[8] A. I. Farrer *et al.*, "Characterization and evaluation of tissue-mimicking gelatin phantoms for use with MRgFUS," *J. Ther. ultrasound*, vol. 3, p. 9, Jun. 2015.

[9] C. Marmorat, A. Arinstein, N. Koifman, Y. Talmon, E. Zussman, and M. Rafailovich, "Cryo-imaging of hydrogels supermolecular structure," *Sci. Rep.*, vol. 6, p. 25495, 2016.

[10] J. P. R. O. Orgel, T. C. Irving, A. Miller, and T. J. Wess, "Microfibrillar structure of type I collagen in situ," *Proc. Natl. Acad. Sci.*, vol. 103, no. 24, pp. 9001–9005, 2006.

[11] G. Menzl *et al.*, "Molecular mechanism for cavitation in water under tension," *Proc. Natl. Acad. Sci.*, vol. 113, no. 48, pp. 13582–13587, 2016.

[12] C. A. Stan *et al.*, "Negative pressures and spallation in water drops subjected to nanosecond shock waves," *J. Phys. Chem. Lett.*, vol. 7, no. 11, pp. 2055–2062, 2016.

[13] B. M. Borkent, S. Gekle, A. Prosperetti, and D. Lohse, "Nucleation threshold and deactivation mechanisms of nanoscopic cavitation nuclei," *Phys. Fluids*, vol. 21, no. 10, p. 102003, Oct. 2009.

[14] R. Gaudron, M. T. Warnez, and E. Johnsen, "Bubble dynamics in a viscoelastic medium with nonlinear elasticity," *J. Fluid Mech.*, vol. 766, pp. 54–75, 2015.

[15] P. O. Kuzema, O. N. Stavinskaya, I. V Laguta, and O. A. Kazakova, "Thermogravimetric study of water affinity of gelatin materials," *J. Therm. Anal. Calorim.*, vol. 122, no. 3, pp. 1231–1237, 2015.

[16] J. H. Johnston and G. T. Peard, "The Surface Tension of Gelatin Solutions," *Biochem. J.*, vol. 19, no. 2, pp. 281–289, 1925.

[17] S. Soleman, M. A. Filippov, A. Dityatev, and J. W. Fawcett, "Targeting the neural extracellular matrix in neurological disorders," *Neuroscience*, vol. 253, pp. 194–213, 2013.

[18] J. C. Fisher, "The fracture of liquids," *J. Appl. Phys.*, vol. 19, no. 11, pp. 1062–1067, 1948.

[19] F. Caupin, "Liquid-vapor interface, cavitation, and the phase diagram of water," *Phys. Rev. E*, vol. 71, no. 5, p. 51605, 2005.

[20] P. Wang, W. Gao, J. Wilkerson, K. M. Liechti, and R. Huang, "Cavitation of water by volume-controlled

stretching," *Extrem. Mech. Lett.*, vol. 11, pp. 59–67, Feb. 2017.

[21] M. E. M. Azouzi, C. Ramboz, J.-F. Lenain, and F. Caupin, "A coherent picture of water at extreme negative pressure," *Nat. Phys.*, vol. 9, no. 1, p. 38, 2013.

[22] E. Herbert, S. Balibar, and F. Caupin, "Cavitation pressure in water," *Phys. Rev. E*, vol. 74, p. 41603, 2006.

[23] P. A. Quinto-Su and K. Ando, "Nucleating bubble clouds with a pair of laser-induced shocks and bubbles," *J. Fluid Mech.*, vol. 733, 2013.

[24] T. D. Wheeler and A. D. Stroock, "The transpiration of water at negative pressures in a synthetic tree," *Nature*, vol. 455, no. 7210, p. 208, 2008.

[25] A. Arvengas, K. Davitt, and F. Caupin, "Fiber optic probe hydrophone for the study of acoustic cavitation in water," *Rev. Sci. Instrum.*, vol. 82, no. 3, p. 34904, 2011.

[26] J. B. Estrada, C. Barajas, D. L. Henann, E. Johnsen, and C. Franck, "High strain-rate soft material characterization via inertial cavitation," *J. Mech. Phys. Solids*, vol. 112, pp. 291–317, Mar. 2018.

[27] C. W. N. Cumper and A. E. Alexander, "The viscosity and rigidity of gelatin in concentrated aqueous systems. I. Viscosity," *Aust. J. Chem.*, vol. 5, no. 1, pp. 146–152, 1952.

[28] H. Yang and Y. Wang, "Effects of concentration on nanostructural images and physical properties of gelatin from channel catfish skins," *Food Hydrocoll.*, vol. 23, no. 3, pp. 577–584, 2009.

[29] A. R. Mackie, A. P. Gunning, M. J. Ridout, and V. J. Morris, "Gelation of gelatin observation in the bulk and at the air-water interface," *Biopolym. Orig. Res. Biomol.*, vol. 46, no. 4, pp. 245–252, 1998.

[30] S. H. Min and M. L. Berkowitz, "Bubbles in water under stretch-induced cavitation," *J. Chem. Phys.*, vol. 150, no. 5, p. 54501, 2019.

[31] I. J. D. Ferry and J. E. Eldridge, "Studies of the Cross-Linking Process in Gelatin Gels.," *J. Phys. Chem.*, vol. 53, no. 1, pp. 184–196, 1949.

[32] T. H. Wen, D. K. Binder, I. M. Ethell, and K. A. Razak, "The perineuronal 'safety' net? Perineuronal net abnormalities in neurological disorders," *Front. Mol. Neurosci.*, vol. 11, p. 270, 2018.

[33] J. R. E. Fraser, T. C. Laurent, and U. B. G. Laurent, "Hyaluronan: its nature, distribution, functions and turnover," *J. Intern. Med.*, vol. 242, no. 1, pp. 27–33, 1997.

[34] R. Frischknecht and C. I. Seidenbecher, "The crosstalk of hyaluronan-based extracellular matrix and synapses," *Neuron Glia Biol.*, vol. 4, no. 3, pp. 249–257, 2008.

[35] D. Carulli, "Perineuronal Nets: A Mechanism to Control Brain Plasticity," 2018.

[36] A. C. McKee and M. E. Robinson, "Military-related traumatic brain injury and neurodegeneration," *Alzheimer's Dement.*, vol. 10, pp. S242–S253, 2014.

[37] P. W. Schofield, G. Logroscino, H. F. Andrews, S. Albert, and Y. Stern, "An association between head circumference and Alzheimer's disease in a population-based study of aging and dementia," *Neurology*, vol. 49, no. 1, pp. 30–37, 1997.

[38] R. Kfoury, B. Marzban, E. Makki, M. L. Greenfield, and H. Yuan, "Effect of pressure profile of shock waves on lipid membrane deformation," *PLoS One*, vol. 14, no. 2, 2019.

[39] D. Sun, X. Lin, Z. Zhang, and N. Gu, "Impact of shock-induced lipid nanobubble collapse on a phospholipid membrane," *J. Phys. Chem. C*, vol. 120, no. 33, pp. 18803–18810, 2016.

[40] K. Koshiyama, T. Kodama, T. Yano, and S. Fujikawa, "Molecular dynamics simulation of structural changes of lipid bilayers induced by shock waves: Effects of incident angles," *Biochim. Biophys. Acta (BBA)-Biomembranes*, vol. 1778, no. 6, pp. 1423–1428, 2008.

[41]   S. Kundu and A. J. Crosby, "Cavitation and fracture behavior of polyacrylamide hydrogels," *Soft Matter*, vol. 5, no. 20, pp. 3963–3968, 2009.

[42]   C. Franck, "Microcavitation: the key to modeling blast traumatic brain injury?" Future Medicine, 2017.

[43]   C. Stewart, S. Center, and C. Stewart, "Blast Injuries" True Weapons of Mass Destruction"," *Work*, vol. 918, pp. 660–2828, 2009.

[44]   Y. Chen, W. Huang, and S. Constantini, "Blast shock wave mitigation using the hydraulic energy redirection and release technology," *PLoS One*, vol. 7, no. 6, p. e39353, 2012.

[45]   M. Tuckerman, *Statistical mechanics: theory and molecular simulation*. Oxford university press, 2010.

[46]   A. D. MacKerell Jr *et al.*, "All-atom empirical potential for molecular modeling and dynamics studies of proteins," *J. Phys. Chem. B*, vol. 102, no. 18, pp. 3586–3616, 1998.

[47]   W. D. Cornell *et al.*, "A second generation force field for the simulation of proteins, nucleic acids, and organic molecules," *J. Am. Chem. Soc.*, vol. 117, no. 19, pp. 5179–5197, 1995.

[48]   C. Oostenbrink, A. Villa, A. E. Mark, and W. F. Van Gunsteren, "A biomolecular force field based on the free enthalpy of hydration and solvation: the GROMOS force-field parameter sets 53A5 and 53A6," *J. Comput. Chem.*, vol. 25, no. 13, pp. 1656–1676, 2004.

[49]   W. L. Jorgensen and J. Tirado-Rives, "The OPLS [optimized potentials for liquid simulations] potential functions for proteins, energy minimizations for crystals of cyclic peptides and crambin," *J. Am. Chem. Soc.*, vol. 110, no. 6, pp. 1657–1666, 1988.

[50]   A. C. T. Van Duin, S. Dasgupta, F. Lorant, and W. A. Goddard, "ReaxFF: a reactive force field for hydrocarbons," *J. Phys. Chem. A*, vol. 105, no. 41, pp. 9396–9409, 2001.

[51]   J. Huang *et al.*, "CHARMM36m: an improved force field for folded and intrinsically disordered proteins," *Nat. Methods*, vol. 14, no. 1, p. 71, 2017.

[52]   S. Jo, T. Kim, V. G. Iyer, and W. Im, "CHARMM-GUI: a web-based graphical user interface for CHARMM," *J. Comput. Chem.*, vol. 29, no. 11, pp. 1859–1865, 2008.

[53]   A. Gautieri, S. Vesentini, A. Redaelli, and M. J. Buehler, "Hierarchical structure and nanomechanics of collagen microfibrils from the atomistic scale up," *Nano Lett.*, vol. 11, no. 2, pp. 757–766, 2011.

[54]   E. F. Pettersen *et al.*, "UCSF Chimera—a visualization system for exploratory research and analysis," *J. Comput. Chem.*, vol. 25, no. 13, pp. 1605–1612, 2004.

[55]   C. Rycroft, "Voro++: A three-dimensional Voronoi cell library in C++," Lawrence Berkeley National Lab.(LBNL), Berkeley, CA (United States), 2009.

[56]   S. Plimpton, "Fast parallel algorithms for short-range molecular dynamics," *J. Comput. Phys.*, vol. 117, no. 1, pp. 1–19, 1995.

[57]   M. J. Abraham *et al.*, "GROMACS: High performance molecular simulations through multi-level parallelism from laptops to supercomputers," *SoftwareX*, vol. 1, pp. 19–25, 2015.

[58]   A. Stukowski, "Visualization and analysis of atomistic simulation data with OVITO–the Open Visualization Tool," *Model. Simul. Mater. Sci. Eng.*, vol. 18, no. 1, p. 15012, 2009.

[59]   W. Humphrey, A. Dalke, and K. Schulten, "VMD: visual molecular dynamics," *J. Mol. Graph.*, vol. 14, no. 1, pp. 33–38, 1996.

[60]   J. Schindelin *et al.*, "Fiji: an open-source platform for biological-image analysis," *Nat. Methods*, vol. 9, no. 7, p. 676, 2012.

[61]   V. P. Skripov, R. Kondor, and D. Slutzkin, *Metastable liquids*, vol. 6. Wiley New York, 1974.

[62] A. M. Stein, D. A. Vader, D. A. Weitz, and L. M. Sander, "The micromechanics of three-dimensional collagen-I gels," *Complexity*, vol. 16, no. 4, pp. 22–28, 2011.

[63] N. B. Vargaftik, B. N. Volkov, and L. D. Voljak, "International tables of the surface tension of water," *J. Phys. Chem. Ref. Data*, vol. 12, no. 3, pp. 817–820, 1983.

[64] K. R. Harris and L. A. Woolf, "Temperature and volume dependence of the viscosity of water and heavy water at low temperatures," *J. Chem. Eng. Data*, vol. 49, no. 4, pp. 1064–1069, 2004.

[65] D. Bhatt, J. Newman, and C. J. Radke, "Molecular dynamics simulations of surface tensions of aqueous electrolytic solutions," *J. Phys. Chem. B*, vol. 108, no. 26, pp. 9077–9084, 2004.

[66] M. A. González and J. L. F. Abascal, "The shear viscosity of rigid water models," *J. Chem. Phys.*, vol. 132, no. 9, p. 96101, 2010.

[67] H. Wadell, "Volume, shape, and roundness of quartz particles," *J. Geol.*, vol. 43, no. 3, pp. 250–280, 1935.

[68] D. A. Head, A. J. Levine, and F. C. MacKintosh, "Distinct regimes of elastic response and deformation modes of cross-linked cytoskeletal and semiflexible polymer networks," *Phys. Rev. E*, vol. 68, no. 6, p. 61907, 2003.

[69] R. C. Tolman, "The effect of droplet size on surface tension," *J. Chem. Phys.*, vol. 17, no. 3, pp. 333–337, 1949.

[70] M. N. Joswiak, R. Do, M. F. Doherty, and B. Peters, "Energetic and entropic components of the Tolman length for mW and TIP4P/2005 water nanodroplets," *J. Chem. Phys.*, vol. 145, no. 20, p. 204703, 2016.

[71] M. N. Joswiak, N. Duff, M. F. Doherty, and B. Peters, "Size-dependent surface free energy and Tolman-corrected droplet nucleation of TIP4P/2005 water," *J. Phys. Chem. Lett.*, vol. 4, no. 24, pp. 4267–4272, 2013.

[72] C. E. Brennen, *[1] C. E. Brennen, Cavitation and Bubble Dynamics. 1995.Cavitation and Bubble Dynamics*. 1995.

[73] M. Strasberg, "The pulsation frequency of nonspherical gas bubbles in liquids," *J. Acoust. Soc. Am.*, vol. 25, no. 3, pp. 536–537, 1953.

[74] M. Morioka, "Measurements of natural frequency and damping constant of single steam bubble oscillating in water," *J. Nucl. Sci. Technol.*, vol. 20, no. 10, pp. 832–843, 1983.

[75] Y. Rotbaum, G. Parvari, Y. Eichen, and D. Rittel, "Linear and Nonlinear Shock Attenuation of Aqueous Methylcellulose Solutions," *Int. J. Impact Eng.*, vol. 136, p. 103392, 2020.

[76] F. Caupin and E. Herbert, "Cavitation in water: A review," *C. R. Phys.*, vol. 7, p. 1000, 2006.

[77] C. E. Brennen, *Cavitation and bubble dynamics*. Cambridge University Press, 2014.

[78] L. G. Gonzalez and T. J. Wess, "The effects of hydration on the collagen and gelatine phases within parchment artefacts," *Herit. Sci.*, vol. 1, no. 1, p. 14, 2013.

[79] C. W. Barney *et al.*, "Cavitation in soft matter," *Proc. Natl. Acad. Sci.*, vol. 117, no. 17, pp. 9157–9165, Apr. 2020.

[80] K. A. H. Al Mahmud, F. Hasan, M. I. Khan, and A. Adnan, "on the Molecular Level cavitation in Soft Gelatin Hydrogel," *Sci. Rep.*, vol. 10, no. 1, pp. 1–13, 2020.

[81] I. Streeter and N. H. de Leeuw, "A molecular dynamics study of the interprotein interactions in collagen fibrils," *Soft Matter*, vol. 7, no. 7, pp. 3373–3382, Apr. 2011.

[82] E. Guillaud, S. Merabia, D. de Ligny, and L. Joly, "Decoupling of viscosity and relaxation processes in supercooled water: a molecular dynamics study with the TIP4P/2005f model," *Phys. Chem. Chem. Phys.*, vol. 19, no. 3, pp. 2124–2130, 2017.

[83] E. H. Grant, "Relationship between relaxation time and viscosity for water," *J. Chem. Phys.*, vol. 26, no. 6, pp. 1575–1577, 1957.

[84] S. Vajda *et al.*, "New additions to the C lus P ro server motivated by CAPRI," *Proteins Struct. Funct. Bioinforma.*, vol. 85, no. 3, pp. 435–444, 2017.

[85] D. Kozakov *et al.*, "How good is automated protein docking?," *Proteins Struct. Funct. Bioinforma.*, vol. 81, no. 12, pp. 2159–2166, 2013.

[86] D. Carulli, "Perineuronal Nets: A Mechanism to Control Brain Plasticity," *The Scientists*, Mar-2018.

[87] S. Jo, K. C. Song, H. Desaire, A. D. MacKerell Jr, and W. Im, "Glycan Reader: automated sugar identification and simulation preparation for carbohydrates and glycoproteins," *J. Comput. Chem.*, vol. 32, no. 14, pp. 3135–3141, 2011.

[88] S. Banerji *et al.*, "Structures of the Cd44–hyaluronan complex provide insight into a fundamental carbohydrate-protein interaction," *Nat. Struct. Mol. Biol.*, vol. 14, no. 3, pp. 234–239, 2007.

[89] G. W. J. McIntosh, "Calculating shock Hugoniots with LAMMPS," 2016.

[90] R. Ravelo, T. C. Germann, O. Guerrero, Q. An, and B. L. Holian, "Shock-induced plasticity in tantalum single crystals: Interatomic potentials and large-scale molecular-dynamics simulations," *Phys. Rev. B*, vol. 88, no. 13, p. 134101, 2013.

[91] O. Guerrero-Miramontes, "1.1 Uniaxial compression in Copper (SCRIPT1)."

[92] Y.-T. Wu and A. Adnan, "Effects of Bubble Size and Gas Density on the Shock-induced Collapse of Nanoscale Cavitation Bubble," *Multiscale Sci. Eng.*, pp. 1–8, 2020.

[93] U. Adhikari, A. Goliaei, and M. L. Berkowitz, "Mechanism of membrane poration by shock wave induced nanobubble collapse: A molecular dynamics study," *J. Phys. Chem. B*, vol. 119, no. 20, pp. 6225–6234, 2015.

[94] N. Bremond, M. Arora, S. M. Dammer, and D. Lohse, "Interaction of cavitation bubbles on a wall," *Phys. Fluids*, vol. 18, p. 121505, 2006.

[95] A. Y. Abuelfilat *et al.*, "Bridging structure and mechanics of three-dimensional porous hydrogel with X-ray ultramicroscopy and atomic force microscopy," *RSC Adv.*, vol. 5, no. 78, pp. 63909–63916, 2015.

[96] C. Vega and E. De Miguel, "Surface tension of the most popular models of water by using the test-area simulation method," *J. Chem. Phys.*, vol. 126, no. 15, p. 154707, 2007.

[97] H. Ogawa, Y. Shiraishi, K. Kawamura, and T. Yokokawa, "Molecular dynamics study on the shear viscosity of molten Na2O·2SiO2," *J. Non. Cryst. Solids*, vol. 119, no. 2, pp. 151–158, Apr. 1990.

Biographical Information

Khandakar Mahmud was born in Rangpur, BANGLADESH on February 04, 1988. He spent his entire childhood in his hometown and finished his Secondary School Certification (equivalent to 10th Grade) and Higher Secondary school Certificate (equivalent to 12th Grade) from Rangpur Cadet College in 2004 and 2006, respectively. In 2007, he moved to the Capital, Dhaka where he began his undergraduate studies at Bangladesh University of Engineering and Technology (BUET) which is considered as the top engineering institution in the nation. In April 2012, he completed his bachelor's degree in Materials and Metallurgical Engineering from BUET. Then, in August of 2012, he began studies for his Master of Science in Mechanical Engineering degree from University of Malaya, Kuala Lumpur under the guidance of Professor Abul Kalam. His M.S. work was related to the tribological characterization of Diamond Like Carbon coating. His Master's work was completed in May of 2015. He then started work on his Doctor of Philosophy in Mechanical Engineering degree from University of Texas at Arlington under the guidance of Dr. Ashfaq Adnan, the American Society of Mechanical Engineers (ASME) fellow professor. Mechanics of soft materials under shock induced loading and bubble growth phenomena by atomistic simulation was his focus. Khandakar completed his PhD in August of 2020.